Journal of Sound and Vibration 455 (2019) 275–298

Contents lists available at ScienceDirect

Journal of Sound and Vibration

journal homepage: www.elsevier.com/locate/jsvi

Multilayer modeling of thermoacoustic sound generation for thermophone analysis and design

Pierre Guiraud [a,b,*], Stefano Giordano [a], Olivier Bou-Matar [a], Philippe Pernod [a], Raphael Lardat [b]

[a] Univ. Lille, CNRS, Centrale Lille, ISEN, Univ. Valenciennes, UMR 8520 - IEMN, LIA LICS/LEMAC, F-59000 Lille, France
[b] Thales Underwater System France, Sophia Antipolis, 525 Route des Dolines, F-06560 Valbonne, France

ARTICLE INFO

Article history:
Received 26 November 2018
Revised 8 April 2019
Accepted 1 May 2019
Available online 13 May 2019
Handling Editor: O. Guasch

Keywords:
Thermoacoustics
Thermophone
Sound generation
Nanomaterials

ABSTRACT

A general model for thermoacoustic sound generation, based on the classical conservation laws of mass, momentum and energy, is presented and adopted to analyze different thermophone structures. This model is able to describe an arbitrary multilayered (or laminated) system composed of both solid and fluid layers. In each layer, we consider the propagation of thermal and acoustic plane waves with a full thermo-visco-elastic coupling and with both thermal and viscous dissipations. In order to obtain a flexible model, useful for most of thermophone systems, the balance equations are written in a general and adaptable matrix form. By adding the continuity of temperature, particle velocity, normal stress and heat flux between the layers, we obtain a closed system of equations, which allows for the calculation of all the acoustic variables at any position and for any input frequency and power. The proposed technique is then applied to several thermophone architectures working in air or in water, and the results are discussed and compared to those of some recent theoretical and experimental investigations. Finally, the approach elaborated here is useful for unifying various theories proposed for distinct thermophone systems and to generalize these approaches in terms of different geometrical and physical features.

1. Introduction

Electroacoustic transducers are the most common and widely used devices to generate sound. They make use of a coil/magnet core to induce the vibration of a membrane system, eventually generating sound waves. On the other hand, piezoelectric devices are typically used for specific applications like, e.g., underwater sound generation in sonars. The efficiency of these transducers have been largely proven but, unfortunately, they generate sound with a mechanical vibration, which is a resonant mechanism. If the use of multiple drivers and filters allows to achieve an almost wideband generation, no simple non-resonant alternative devices are currently available. A possible solution could be obtained by means of the thermoacoustic effect. This is based on the application of an oscillating electric current to an electrical conducting material with a high thermal conductivity and a low thermal capacity. The result is that the temperature evolution of the sample accurately follows the applied current profile. Consequently, the compression/dilatation of the air in contact to the surface of the material generates

* Corresponding author. Cité Scientifique, Avenue Henri Poincaré, CS 60069, 59 652 Villeneuve d'Ascq Cedex, France.
E-mail addresses: pierre.guiraud@centraliens-lille.org (P. Guiraud), stefano.giordano@univ-lille.fr (S. Giordano), olivier.bou-matar@univ-lille.fr (O. Bou-Matar), philippe.pernod@univ-lille.fr (P. Pernod), raphael.lardat@fr.thalesgroup.com (R. Lardat).

https://doi.org/10.1016/j.jsv.2019.05.001
0022-460X/

an acoustic wave whose frequency is proportional to the input frequency of the electric current. Since no resonating part are involved in the process, the generation is wideband.

In the first decades of the twentieth century, the thermoacoustic effect has been firstly exploited in the works of de Lange [1] and of Arnold and Crandall [2] to design precise sources of sound. Successively, their theoretical and experimental activities have been further improved by Wente [3,4]. However, at that time, the limitations in terms of relevant thermophone materials have prevented the perpetuation of this research line. More recently, a work by Shinoda et al. discussed a thermoacoustic device based on a 30 nm thick aluminum film deposited on a porous silicon layer [5]. The analysis of this system greatly promoted the interest for the thermoacoustic effect and its applications. Indeed, the advent of nanomaterials and nanotechnologies allows the development of new nanostructured materials to be used as thermophones. For instance, recent investigations are based on carbon nanotubes [6,7], aluminum wires [8], gold wires [9], silver wires [10] and also carbon based structures such as 2D graphene paper [11] and 3D graphene foam [12,13].

From the theoretical point of view, most analyses of the thermophone principle used the so-called *piston based model*. These approaches are based on a heat flow balance equation taking into account the convection, the conduction, the radiation losses and the heat stored in the material. The first attempt to use this method to model a thermophone in free field was done by Arnold and Crandall in their pioneering investigation, where however they neglected the heat stored within the thermophone [2]. This term was recently added in the investigation performed by Xiao et al. [14]. Then, Daschewski et al. used the heat flow balance equation by adding the influence of a substrate (or backing) on the thermophone response, and the effect of the viscous dissipation in the propagation medium [15,16]. In the following, this approach was successfully used by Kim et al. to describe the behavior of a graphene thermophone deposited on a polymer-mesh substrate [17]. Successively, La Torraca et al. added conduction and convection contributions to the model and also took the thickness of the substrate into account [18]. The *piston based models* are accurate in many cases but have limitations depending on the input parameters and the geometry of the system (especially at high frequencies).

Another approach used for modeling the thermoacoustic effect is based on the classical conservation laws of continuum mechanics applied to a propagation medium (typically without viscosity). These equations were elaborated by MacDonald et al. for studying the photoacoustic effect [19]. More recently, the same set of equations has been adopted also for the thermoacoustics analysis. This coupled set of equations was firstly solved by Hu et al. for a thermophone placed on a substrate, generating sound in a perfect gas [20]. This model was validated against Shinoda's experimental data [5], and was later adapted to evaluate the far field pressure and to consider the influence of the so-called *heat capacity* per *unit area* (HCPUA) [11]. Moreover, this approach was modified to investigate a spherical geometry of the thermophone (acoustic monopole) [21], and also generalized to arbitrary sources [22]. The same set of equations has been considered for a cylindrical geometry of the thermophone as well [23]. A refined analysis of this methodology has been performed to study the influence of the main thermophone parameters on its wideband frequency response [24].

An investigation proposed to merge the equations of the continuum mechanics with the thermal balance of the piston based model [25]. This idea was applied to a free field configuration, eventually leading to a good agreement with experimental results (obtained in Ref. [14]). Based on this work, Tong et al. added the influence of an air gap between the thermophone and a substrate, which represents a promising technique to improve the thermophone efficiency [26]. A generalized theory was developed to describe point source, line source and line array thin film thermophones in free field and in half space with an air gap over the substrate [27]. Also, the properties of nanoscale thermophones have been studied by Vesterinen et al., eventually obtaining generic ultimate limits for the thermophone efficiency [28]. The theory was confirmed against experiments and finite difference method simulations. This model was later improved by Brown et al. [29] by considering line thermophones of finite length.

The thermoacoustic sound generation has been also extended to underwater applications. In particular, Aliev et al. investigated the response of a carbon nanotube projector placed in water [30]. They provided evidence that the hydrophobicity of the nanotubes in water generates an air layer around the nanotubes that increases the pressure generation efficiency of the thermophone. Other studies concerned the use of encapsulated thermophone systems, developed in order to obtain a protection from the liquid medium [31,32]. These results may be compared with the response of carbon nanotube thin films in a variety of gaseous media [31,33].

Each of the above summarized models has been developed to describe the behavior of a specific thermophone configuration with well defined identifying characteristics. Moreover, in each model some physical features have been neglected to simplify the analysis, and to obtain explicit results. For instance, the viscosity of the propagation medium is not considered in these models except for the work by Daschewski et al., as mentioned above [15,16]. In addition, these models do not consider the acoustic wave propagation within the active solid layers. Therefore, the influence of potential resonances within the solid layers is not investigated in the literature. If sometimes mentioned [29], resonances are assumed to be in a frequency range higher than the one of interest. Nonetheless, knowing that the efficiency of thermophones can be improved using high frequency pulse modulation [34], it is important to understand the possible limitations of this technique.

Grounded on previous arguments, the model elaborated in this work describes an arbitrary multilayered structure where each layer can be either a solid (e.g. representing the thermophone material or other components of the device), or a fluid (e.g., representing the propagation medium or a gap in the system). Doing so, we developed a flexible and adaptable methodology, which can be easily applied to the analysis of any thermophone structure without the need to elaborate the pertinent equations in each particular case. In the present model a set of coupled differential equations (full thermo-visco-elastic coupling) will be solved for plane waves (planar thermophone geometry) in any fluid and solid layer. It means that each layer is modeled by taking into account both the thermal and the viscous dissipation. It can be noted that we rewrote the basic equations

of continuum mechanics in the same mathematical form for the one-dimensional behavior of both solid and fluid materials, thus strongly simplifying the implementation of the procedure. The general solution, giving the relevant physical fields in any layer, will be presented in matrix form, allowing for the easy calculation of sound pressure in any thermophone configuration. The plane waves propagation is fully considered in both fluid and solid layers and, therefore, one can thoroughly analyze the possible resonances of any thermophone structure. This model will be compared with the theoretical results of some of the above mentioned models to illustrate the relevance and flexibility of this new approach. Moreover, in order to validate our approach, other comparisons will be drawn with experimental results of the recent literature. Finally, novel configurations for the thermoacoustic sound generation in air and water are explored and discussed.

2. Theoretical formalism: balance equations

The proposed model for the thermoacoustic sound generation is based on a multilayered structure, where each layer is either composed by a solid material (representing an active region, a substrate or other components of the generation system) or made of a fluid medium (typically air or water, representing a region subject to acoustic propagation). In this system of layers we fully describe the heat transfer and the mechanical waves propagation by also taking into account dissipative phenomena described by the viscosity of involved materials. To this aim, we define here the main balance equations considered for both solid and fluid layers. Concerning the fluid layers, the set of equations on which our model is based takes account of the conservation of mass, momentum and energy written as [35].

$$\begin{aligned} \frac{1}{B}\frac{\partial p}{\partial t} &= \alpha_T \frac{\partial T}{\partial t} - \vec{\nabla}\cdot\vec{v}, \\ \rho\frac{\partial \vec{v}}{\partial t} &= -\vec{\nabla}p + \mu\nabla^2\vec{v} + (\lambda+\mu)\vec{\nabla}(\vec{\nabla}\cdot\vec{v}), \\ \rho C_p\frac{\partial T}{\partial t} &= \kappa\nabla^2 T + \alpha_T T_0\frac{\partial p}{\partial t}, \end{aligned} \tag{1}$$

where the pressure p (Pa), the temperature variation T (K) and the particle velocity vector $\vec{v}$ (m/s) are the main variables depending on time t (s) and space $\vec{r}$ (m). Moreover, ρ is the density (kg/m^3), B the Bulk Modulus (Pa), α_T the coefficient of volumetric expansion (1/K), λ and μ the first and second viscosity coefficients (Pa·s), C_p the specific heat at constant pressure (J/(kg·K)), T_0 the ambient temperature (K) and, finally, κ the thermal conductivity (W/(m·K)). All these parameters will be considered as constants in each layer, and they can only vary from one layer to another. It is important to remark that the balance equations given in Eq. (1) represent the combination of the linearized classical conservation laws with the linearized constitutive equations of the material. This linearization can be easily justified in our context since thermo-acoustic waves are usually represented by small variations of the relevant quantities around given equilibrium values. As an example, T is the variation of temperature with respect to its equilibrium value T_0 (the actual temperature being equal to $T + T_0$).

A similar set of equations can be written in a solid layer by taking into consideration the particle displacement vector $\vec{u}$ (m), the Lamé elastic coefficients λ_0 and μ_0 (Pa), the specific heat at constant volume C_v (J/kg·K), the externally applied body forces $\vec{b}$ (N) and the supplied thermal power density S_0 (W/m^3). The classical continuum mechanics delivers [36].

$$\begin{aligned} \rho\frac{\partial^2\vec{u}}{\partial t^2} &= (\lambda_0+\mu_0)\vec{\nabla}(\vec{\nabla}\cdot\vec{u}) + \mu_0\nabla^2\vec{u} + \vec{b} + (\lambda+\mu)\vec{\nabla}(\vec{\nabla}\cdot\vec{v}) + \mu\nabla^2\vec{v} - \alpha_T B\vec{\nabla}T, \\ \rho C_v\frac{\partial T}{\partial t} &= \kappa\nabla^2 T - \alpha_T B\frac{\partial}{\partial t}\vec{\nabla}\cdot\vec{u}\,T_0 + S_0, \end{aligned} \tag{2}$$

which is the system of equations governing the thermo-elasticity under the hypotheses of small deformation $\hat{\varepsilon} = 1/2(\vec{\nabla}\vec{u} + \vec{\nabla}\vec{u}^T)$ and small temperature variations T around T_0. While the first equation represents the momentum conservation, the second one describes the energy balance. We remark that in the solid layers we always have $\vec{v} = \partial\vec{u}/\partial t$ and $B = \lambda_0 + (2/3)\mu_0$. Furthermore, we underline that the power density S_0, entering the active solid layer, will represent the energy supplied to the system and converted into acoustical wave through the thermoacoustic coupling. Typically, S_0 will be generated by Joule effect, induced by an electric current applied to the active layer.

In the following sections, we will apply these equations for the specific case of plane waves propagation. It means that we will study the one-dimensional geometry for an arbitrary system composed of parallel layers of solid or fluid materials. This program will allow us to compare and unify the results obtained in the literature by means of different methods. Indeed, it is important to generalize these approaches in order to consider an arbitrary number of layers, and to take account of the dissipative processes in the acoustic generation and propagation. We underline that the propagation of waves in the solid layers is a point systematically neglected in the literature. We also remark that the cases of cylindrical and spherical waves could be thoroughly studied by means of our approach but, for the sake of brevity, we do not discuss this issue here.

2.1. Plane wave propagation in a fluid layer

Assuming plane wave propagation in the x direction, within a fluid layer, Eq. (1) becomes

$$\begin{aligned}\frac{1}{B}\frac{\partial p}{\partial t} &= \alpha_T \frac{\partial T}{\partial t} - \frac{\partial v}{\partial x},\\ \rho\frac{\partial v}{\partial t} &= -\frac{\partial p}{\partial x} + (\lambda+2\mu)\frac{\partial^2 v}{\partial x^2},\\ \rho C_p \frac{\partial T}{\partial t} &= \kappa\frac{\partial^2 T}{\partial x^2} + \alpha_T T_0 \frac{\partial p}{\partial t}.\end{aligned} \tag{3}$$

We also assume the harmonic time dependence for the variables p, v, T. Hence, we can apply the formal substitution $\partial/\partial t \to \mathrm{i}\omega$, $\partial/\partial x \to \mathrm{d}/\mathrm{d}x$, and the system takes the form

$$\begin{aligned}\mathrm{i}\omega\frac{1}{B}p &= \mathrm{i}\omega\alpha_T T - \frac{\mathrm{d}v}{\mathrm{d}x},\\ \mathrm{i}\omega\rho v &= -\frac{\mathrm{d}p}{\mathrm{d}x} + (\lambda+2\mu)\frac{\mathrm{d}^2 v}{\mathrm{d}x^2},\\ \mathrm{i}\omega\rho C_p T &= \kappa\frac{\mathrm{d}^2 T}{\mathrm{d}x^2} + \mathrm{i}\omega\alpha_T T_0 p.\end{aligned} \tag{4}$$

The first equality in Eq. (4) gives the pressure as

$$p = \alpha_T B T - \frac{B}{\mathrm{i}\omega}\frac{\mathrm{d}v}{\mathrm{d}x}. \tag{5}$$

Now, by substituting Eq. (5) into the other two equalities of Eq. (4), and by using the relationship between the specific heats

$$\rho(C_p - C_v) = T_0\alpha_T^2 B, \tag{6}$$

the velocity v as a function of the temperature T is eventually obtain as

$$v = -\frac{1}{\mathrm{i}\omega\rho}\left[\alpha_T B + \frac{\mathrm{i}\omega\rho C_v}{\alpha_T T_0 B}(\lambda+2\mu+\frac{B}{\mathrm{i}\omega})\right]\frac{\mathrm{d}T}{\mathrm{d}x} + (\lambda+2\mu+\frac{B}{\mathrm{i}\omega})\frac{\kappa}{\mathrm{i}\omega\rho\alpha_T T_0 B}\frac{\mathrm{d}^3 T}{\mathrm{d}x^3}. \tag{7}$$

This allows to find a fourth order biquadratic differential equation for the temperature T

$$(\lambda+2\mu+\frac{B}{\mathrm{i}\omega})\kappa\frac{\mathrm{d}^4 T}{\mathrm{d}x^4} - \left[(\lambda+2\mu+\frac{B}{\mathrm{i}\omega})\mathrm{i}\omega\rho C_v + (\mathrm{i}\omega\rho\kappa + \alpha_T^2 T_0 B^2)\right]\frac{\mathrm{d}^2 T}{\mathrm{d}x^2} - \omega^2\rho^2 C_v T = 0. \tag{8}$$

The general solution of Eq. (8) can be written in the explicit form

$$T = \mathsf{A}\mathrm{e}^{-\mathrm{i}kx} + \mathsf{B}\mathrm{e}^{\mathrm{i}kx} + \mathsf{C}\mathrm{e}^{-\sigma x} + \mathsf{D}\mathrm{e}^{\sigma x}, \tag{9}$$

where the parameters k and σ can be found as described below and A, B, C and D are integration coefficients to be determined through the boundary conditions (see Section 3).

The classical Helmholtz equation in a fluid for an isentropic or adiabatic process (without viscosity and thermal conduction) is $\frac{\mathrm{d}^2 T}{\mathrm{d}x^2} + \frac{\omega^2}{C_0^2}T = 0$, which represent progressive and regressive waves with velocity C_0. As a matter of fact, it can be obtained from Eq. (8) with $\lambda = \mu = 0$ and $\kappa = 0$. For our general case, we aim at rewriting Eq. (8) in terms of C_0. To do this, we introduce here the notations

$$\gamma = \frac{C_p}{C_v}, \tag{10}$$

$$C_0 = \sqrt{\frac{B}{\rho}\gamma}, \tag{11}$$

$$l_\kappa = \frac{C_0\kappa}{BC_p} = \frac{\alpha\gamma}{C_0}, \tag{12}$$

$$l_V = \frac{\lambda+2\mu}{\rho C_0}, \tag{13}$$

where l_k and l_V are characteristic lengths representing the conduction and the viscous processes, respectively (also, $\alpha = \kappa/(\rho C_p)$ is the so-called thermal diffusivity). Therefore, the differential equation for the temperature given in Eq. (8) can be usefully rewritten as

$$l_k(l_V - \mathrm{i}\frac{C_0}{\omega\gamma})\frac{\mathrm{d}^4 T}{\mathrm{d}x^4} - [1 + \mathrm{i}\frac{\omega}{C_0}(l_k + l_V)]\frac{\mathrm{d}^2 T}{\mathrm{d}x^2} - \frac{\omega^2}{C_0^2}T = 0, \tag{14}$$

where the isentropic case can be easily found when $l_k = l_V = 0$.

In order to find simplified explicit expressions for k and σ, defining the solution in Eq. (9), we make the assumption of weak conduction and weak viscosity. Hence, the asymptotic solutions of $ax^4 + bx^2 + c = 0$ for small values of a are investigated. If $a = 0$, the first couple of solutions is given by $x^2 = -\frac{c}{b}$, which means $x = \pm\sqrt{-\frac{c}{b}}$. So, we search ε such that $x = \pm\sqrt{-\frac{c}{b}} + \varepsilon a$, in order to obtain the solutions to the first order in the parameter a. These solutions correspond to a regular perturbation.

However, the second couple of solutions diverges to infinity when $a \to 0$, thus corresponding to a singular perturbation. So, we define $y = \sqrt{a}x$ and $ax^4 + bx^2 + c = 0$ is transformed into $y^4 + by^2 + ac = 0$. If $a = 0$, we get $y = \pm\sqrt{-b}$ and the perturbed solutions are written as $y = \pm\sqrt{-b} + \varepsilon a$.

Now, by substituting the first couple of solutions $x = \pm\sqrt{-\frac{c}{b}} + \varepsilon a$ in $ax^4 + bx^2 + c = 0$, and the second couple $y = \pm\sqrt{-b} + \varepsilon a$ in $y^4 + by^2 + ac = 0$, we can obtain the pertinent values of the first order coefficients ε, and we eventually get the four solutions for small values of a, as follows

$$x_{1,2} = \pm\left[\sqrt{-\frac{c}{b}} - \frac{1}{2}\frac{ac^2}{b^3}\sqrt{-\frac{b}{c}}\right], \tag{15}$$

$$x_{3,4} = \pm\left[\sqrt{-\frac{b}{a}} + \frac{1}{2}\frac{c}{b}\sqrt{-\frac{a}{b}}\right]. \tag{16}$$

If we consider that $\mathrm{Re}(a) > 0$, $\mathrm{Re}(b) < 0$ and $c < 0$ (as in our case, see Eq. (14)), we can easily obtain the simplified forms

$$x_{1,2} = \pm\sqrt{-\frac{c}{b}}\left[1 + \frac{1}{2}\frac{ac}{b^2}\right], \tag{17}$$

$$x_{3,4} = \pm\sqrt{-\frac{b}{a}}\left[1 - \frac{1}{2}\frac{ac}{b^2}\right]. \tag{18}$$

Through these general solutions, the acoustic wavenumber k and the thermal attenuation σ (defined in Eq. (9)) can be approximated to the first order in l_V and l_k by

$$k = \pm\frac{\omega}{C_0}\left[1 - \frac{1}{2}\frac{i\omega}{C_0}l_V - \frac{1}{2}\frac{i\omega}{C_0}l_k(1 - \frac{1}{\gamma})\right], \tag{19}$$

$$\sigma = \pm\sqrt{\frac{i\omega\gamma}{C_0 l_k}}\left[1 + \frac{1}{2}\frac{i\omega}{C_0}l_k(1 - \frac{1}{\gamma}) + \frac{1}{2}\frac{i\omega}{C_0}l_V(1 - \gamma)\right]. \tag{20}$$

It can be noted that $\frac{\gamma}{C_0 l_k} = \frac{C_p\rho}{\kappa} = \frac{1}{\alpha}$ where α is the thermal diffusivity of the medium. This change of parameters allows for a better comparison with the first order wavenumbers found in Hu's paper [20] and shows consistency with the approximated wavenumbers $k = \omega/C_0$ and $\sigma = \sqrt{i\omega\alpha}$, used in most piston models (see Section 4 for details). When k and σ are known, the temperature evolution can be found through Eq. (9) and all the pertinent variables can be deduced from Eqs. (5) and (7).

From Eq. (19), we deduce that the classical progressive acoustic mode $\exp[i\omega(t - x/v_{ac}) - x/\boldsymbol{\mathcal{L}}_{ac}]$ is characterized by a penetration length

$$\boldsymbol{\mathcal{L}}_{ac} = \frac{2C_0^2}{\omega^2}\frac{1}{l_V + \left(1 - \frac{1}{\gamma}\right)l_k}, \tag{21}$$

and by a phase velocity

$$v_{ac} = C_0. \tag{22}$$

It means that the penetration length becomes infinity for isentropic processes ($l_k = l_V = 0$), while the wave velocity is independent of the dissipative phenomena, assuming the value C_0 in any case. On the other hand, from Eq. (20), we understand that the progressive thermal mode $\exp[i\omega(t - x/v_{th}) - x/\boldsymbol{\mathcal{L}}_{th}]$ is designated by a penetration length

$$\boldsymbol{\mathcal{L}}_{th} = \frac{2}{\sqrt{2}}\sqrt{\frac{C_0 l_k}{\omega\gamma}}\left\{1 + \frac{\omega}{2C_0}\left[l_k\left(1 - \frac{1}{\gamma}\right) + l_V(1 - \gamma)\right]\right\}, \tag{23}$$

and by a phase velocity

$$v_{th} = \frac{2\omega}{\sqrt{2}}\sqrt{\frac{C_0 l_k}{\omega\gamma}}\left\{1 - \frac{\omega}{2C_0}\left[l_k\left(1 - \frac{1}{\gamma}\right) + l_V(1 - \gamma)\right]\right\}. \tag{24}$$

To conclude, with weak dissipative processes, we get the classical expression $\boldsymbol{\mathcal{L}}_{th} = \frac{v_{th}}{\omega} = 2\sqrt{\frac{C_0 l_k}{2\omega\gamma}} = \sqrt{\frac{2\alpha}{\omega}}$, often accepted as a good approximation for low values of l_k and l_V [20].

2.2. Plane wave propagation in a solid layer

We consider here Eq. (2) with $\vec{b} = 0$ since we suppose that the solid layer is not subject to external body forces. Therefore, in the one-dimensional case this system of equations can be rewritten as

$$\rho\frac{\partial v}{\partial t} = (\lambda_0 + 2\mu_0)\frac{\partial^2 u}{\partial x^2} + (\lambda + 2\mu)\frac{\partial^2 v}{\partial x^2} - \alpha_T B\frac{\partial T}{\partial x}, \tag{25}$$

$$\rho C_v\frac{\partial T}{\partial t} = \kappa\frac{\partial^2 T}{\partial x^2} - \alpha_T B T_0\frac{\partial^2 u}{\partial t\partial x} + S_0, \tag{26}$$

where $v = \frac{\partial u}{\partial t}$. We aim at rewriting this system of equation in the same form obtained for the fluid in Eq. (3). To do this, we define the pressure as the normal component of the thermoelastic stress tensor (with opposite sign). It means that

$$p = -(2\mu_0 + \lambda_0)\frac{\partial u}{\partial x} + \alpha_T B T. \tag{27}$$

It is important to remark that this definition takes into consideration only the thermoelastic part of the total stress and not its viscous component. Hence, in order to impose the continuity of the normal stress at a given interface, the viscous term must be added to this pressure value. We will make use of this point in Section 3.1 when the continuity of quantities at the boundaries will be of interest to analyze the multilayered structure. Eventually, Eqs. (25) and (26) can be rewritten as

$$\begin{aligned}
\frac{\partial p}{\partial t} &= -(\lambda_0 + 2\mu_0)\frac{\partial v}{\partial x} + \alpha_T B\frac{\partial T}{\partial t},\\
\rho\frac{\partial v}{\partial t} &= -\frac{\partial p}{\partial x} + (\lambda + 2\mu)\frac{\partial^2 v}{\partial x^2},\\
\rho C_v\frac{\partial T}{\partial t} &= \kappa\frac{\partial^2 T}{\partial x^2} - \alpha_T B T_0\frac{\partial v}{\partial x} + S_0.
\end{aligned} \tag{28}$$

If Eqs. (3) and (28) look similar, they are not in the exact same form yet. To further elaborate Eq. (28), we can calculate $\partial v/\partial x$ from the first equation and substitute this result in the third equation, representing the heat transfer law in solid deformable media. Moreover, these equations can be usefully written in terms of the longitudinal and transverse wave velocities v_L and v_T defined as [36].

$$v_L = \sqrt{\frac{\lambda_0 + 2\mu_0}{\rho}}, \qquad v_T = \sqrt{\frac{\mu_0}{\rho}}. \tag{29}$$

By observing that the bulk modulus can be written as $B = \lambda_0 + \frac{2}{3}\mu_0 = \rho(v_L^2 - \frac{4}{3}v_T^2)$, and by using Eq. (6), which is valid for both fluid and solid layers, the system of equations for the plane wave propagation in a solid can be finally written as

$$\begin{aligned}
\frac{\boldsymbol{\mathcal{M}}}{B}\frac{\partial p}{\partial t} &= \alpha_T\boldsymbol{\mathcal{M}}\frac{\partial T}{\partial t} - \frac{\partial v}{\partial x},\\
\rho\frac{\partial v}{\partial t} &= -\frac{\partial p}{\partial x} + (\lambda + 2\mu)\frac{\partial^2 v}{\partial x^2},\\
\rho C_p\boldsymbol{\mathcal{N}}\frac{\partial T}{\partial t} &= \alpha_T\boldsymbol{\mathcal{M}} T_0\frac{\partial p}{\partial t} + \kappa\frac{\partial^2 T}{\partial x^2} + S_0,
\end{aligned} \tag{30}$$

where the coefficients $\boldsymbol{\mathcal{M}}$ and $\boldsymbol{\mathcal{N}}$ have been introduced as follows

$$\boldsymbol{\mathcal{M}} = 1 - \frac{4}{3}\frac{v_T^2}{v_L^2}, \tag{31}$$

$$\boldsymbol{\mathcal{N}} = 1 - \frac{C_p - C_v}{C_p}\frac{4}{3}\frac{v_T^2}{v_L^2}. \tag{32}$$

Comparing now this result with the analogous system for the fluid (see Eq. (3)), its is seen that the set of equations assume the same mathematical form provided that we apply the following change of parameters

$$B^{(f)} = \frac{B^{(s)}}{\boldsymbol{\mathcal{M}}}, \tag{33}$$

$$\alpha_T^{(f)} = \boldsymbol{\mathcal{M}}\alpha_T^{(s)}, \tag{34}$$

$$C_p^{(f)} = \mathcal{N} C_p^{(s)}, \tag{35}$$

$$C_v^{(f)} = C_v^{(s)}, \tag{36}$$

where (f) and (s) stand for fluid and solid, respectively, and where $\mathcal{M}$ and $\mathcal{N}$ are always calculated with the solid properties. Interestingly enough, all parameters remain unchanged if $\nu_T = 0$, a condition effectively characterizing a fluid where only longitudinal waves can propagate (in this case $\nu_T = 0$, or equivalently, $\mathcal{M} = \mathcal{N} = 1$). We remark that this change of parameters gives a fully self-consistent procedure since the following property can be easily proved: we have that $\rho(C_p^{(f)} - C_v^{(f)}) = T_0\left(\alpha_T^{(f)}\right)^2 B^{(f)}$ if and only if $\rho(C_p^{(s)} - C_v^{(s)}) = T_0\left(\alpha_T^{(s)}\right)^2 B^{(s)}$. It means that the parameters transformation introduced preserves the thermodynamic relation, given in Eq. (6), between the specific heats.

The important point is that fluid and solid layers can be now represented by the same set of equations for p, v and T given in Eq. (3), paying attention to apply the change of parameters given in Eqs.(33)-(36) when we consider a solid layer. Of course, this result strongly simplifies the implementation of the procedure for dealing with a multilayered structures. In the case of a solid layer with $S_0 \neq 0$, we have also to add a particular solution in the temperature profile, function of the supplied heat density S_0. More specifically, if S_0 is uniform within the layer, this particular solution of T can be calculated by substituting a constant function in the complete equation for the temperature including the source term. A straightforward calculation delivers

$$T_1 = \frac{S_0}{\mathrm{i}\omega\rho C_v}, \tag{37}$$

which must be added to the homogeneous solution given in Eq. (9), in order to have the complete expression for the temperature variation. Therefore, we can finally write

$$T = \mathsf{A}\mathrm{e}^{-\mathrm{i}kx} + \mathsf{B}\mathrm{e}^{\mathrm{i}kx} + \mathsf{C}\mathrm{e}^{-\sigma x} + \mathsf{D}\mathrm{e}^{\sigma x} + \frac{S_0}{\mathrm{i}\omega\rho C_v}, \tag{38}$$

in each active solid layer of the system.

3. Matrix approach for the multilayered structure

The general solution obtained in the previous Section for a given fluid or solid layer will be exploited here to elaborate a complete procedure able to consider a multilayered system, whose geometry is shown in Fig. 1. The number N of layers can be changed and each layer can be made of a different material, either solid or liquid (air, water, silicon, carbon …). Also the size $l_j - l_{j-1}$ $(\forall j = 2, \dots, N-1)$ of the layers can be changed except for the first and the last ones which are supposed to be semi-infinite and without any input volumetric source. This scheme will be adopted to describe the behavior of different configurations of thermophone devices in the following sections.

3.1. Matrix form of the solution in a given layer

In order to create a flexible representation of the solution for a given layer, we consider the physical quantities that are continuous at any interface, namely the temperature, the normal stress tensor, the particle velocity and the heat flux. It means that we assume ideal interfaces without imperfections and defects. In the case of imperfect interfaces, the continuity equations should be substituted with specific jump condition [37,38]. An example will be given in a next section. Anyway, the number of the continuous quantities is coherent with the number of the undetermined coefficients A, B, C and D, defining Eq. (9). In the one-dimensional case the heat flux q is simply defined as

$$q = -\kappa \frac{\mathrm{d}T}{\mathrm{d}x}. \tag{39}$$

Moreover, the normal stress tensor $\widetilde{p}$ must be considered as the sum of pressure and the viscous normal stress. It follows that

$$\widetilde{p} = p - \mathrm{i}\omega(\lambda + 2\mu)\frac{\mathrm{d}u}{\mathrm{d}x} = p - (\lambda + 2\mu)\frac{\mathrm{d}v}{\mathrm{d}x}. \tag{40}$$

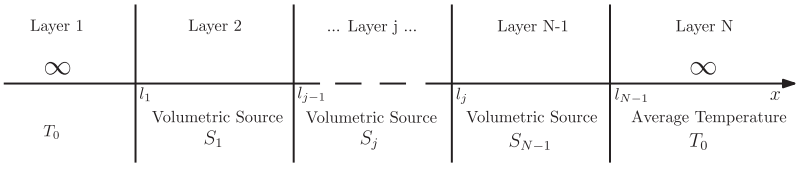

Fig. 1. Schematic of a multilayered structures composed of an arbitrary sequence of fluid and solid layers, able to represent different thermoacoustic sound generation systems. While the first and the last regions are semi-infinite, the others correspond to limited layers between l_{j-1} and $l_j, \forall j = 2, \dots, N-1$.

This is the one-dimensional stress quantity that is continuous at any interface, for both fluid and solid layers. By using Eqs. (9), (7), (5), (39) and (40) the set of solutions in a fluid layer is obtained as

$$\widetilde{p} = \mathsf{A}\boldsymbol{\mathcal{F}}(-\mathrm{i}k)\mathrm{e}^{-\mathrm{i}kx} + \mathsf{B}\boldsymbol{\mathcal{F}}(\mathrm{i}k)\mathrm{e}^{\mathrm{i}kx} + \mathsf{C}\boldsymbol{\mathcal{F}}(-\sigma)\mathrm{e}^{-\sigma x} + \mathsf{D}\boldsymbol{\mathcal{F}}(\sigma)\mathrm{e}^{\sigma x} \tag{41}$$

$$v = \mathsf{A}\mathcal{G}(-\mathrm{i}k)\mathrm{e}^{-\mathrm{i}kx} + \mathsf{B}\mathcal{G}(\mathrm{i}k)\mathrm{e}^{\mathrm{i}kx} + \mathsf{C}\mathcal{G}(-\sigma)\mathrm{e}^{-\sigma x} + \mathsf{D}\mathcal{G}(\sigma)\mathrm{e}^{\sigma x} \tag{42}$$

$$q = \mathsf{A}\kappa\mathrm{i}k\mathrm{e}^{-\mathrm{i}kx} - \mathsf{B}\kappa\mathrm{i}k\mathrm{e}^{\mathrm{i}kx} + \mathsf{C}\kappa\sigma\mathrm{e}^{-\sigma x} - \mathsf{D}\kappa\sigma\mathrm{e}^{\sigma x} \tag{43}$$

$$T = \mathsf{A}\mathrm{e}^{-\mathrm{i}kx} + \mathsf{B}\mathrm{e}^{\mathrm{i}kx} + \mathsf{C}\mathrm{e}^{-\sigma x} + \mathsf{D}\mathrm{e}^{\sigma x}, \tag{44}$$

where we used the functions

$$\boldsymbol{\mathcal{F}}(\eta) = \alpha_T B - \left(\frac{B}{\mathrm{i}\omega} + \lambda + 2\mu\right)(\mathsf{L}_1\eta^2 + \mathsf{L}_2\eta^4), \tag{45}$$

$$\mathcal{G}(\eta) = \mathsf{L}_1\eta + \mathsf{L}_2\eta^3, \tag{46}$$

with L_1 and L_2 being the coefficients of Eq. (7), namely

$$\mathsf{L}_1 = -\frac{1}{\mathrm{i}\omega\rho}\left[\alpha_T B + \frac{\mathrm{i}\omega\rho C_v}{\alpha_T T_0 B}(\lambda + 2\mu - \mathrm{i}\frac{B}{\omega})\right], \tag{47}$$

$$\mathsf{L}_2 = (\lambda + 2\mu - \mathrm{i}\frac{B}{\omega})\frac{\kappa}{\mathrm{i}\omega\rho\alpha_T T_0 B}, \tag{48}$$

so that $v = \mathsf{L}_1\frac{\mathrm{d}T}{\mathrm{d}x} + \mathsf{L}_2\frac{\mathrm{d}^3T}{\mathrm{d}x^3}$. The parameters k and σ are either defined by solving by numerical techniques the fourth degree biquadratic equation associated to Eq. (8) or by using the first order approximations obtained in Eqs. (19) and (20). If we consider the physical parameters of typical materials used in thermoacoustic systems, the difference between the exact and approximated solutions is less than 0.5% in a large frequency range in air. Nevertheless, this assumption do not hold for fluids with higher viscosity (see Section 6.2 for the underwater case). If we define the matrices

$$H^{(a)} = \begin{bmatrix} \boldsymbol{\mathcal{F}}(-\mathrm{i}k) & \boldsymbol{\mathcal{F}}(\mathrm{i}k) & \boldsymbol{\mathcal{F}}(-\sigma) & \boldsymbol{\mathcal{F}}(\sigma) \\ \mathcal{G}(-\mathrm{i}k) & \mathcal{G}(\mathrm{i}k) & \mathcal{G}(-\sigma) & \mathcal{G}(\sigma) \\ \kappa\mathrm{i}k & -\kappa\mathrm{i}k & \kappa\sigma & -\kappa\sigma \\ 1 & 1 & 1 & 1 \end{bmatrix} \tag{49}$$

and

$$H^{(b)}(x) = \begin{bmatrix} \mathrm{e}^{-\mathrm{i}kx} & 0 & 0 & 0 \\ 0 & \mathrm{e}^{\mathrm{i}kx} & 0 & 0 \\ 0 & 0 & \mathrm{e}^{-\sigma x} & 0 \\ 0 & 0 & 0 & \mathrm{e}^{\sigma x} \end{bmatrix} \tag{50}$$

the general solution in a given fluid layer is given by

$$\begin{bmatrix} \widetilde{p} \\ v \\ q \\ T \end{bmatrix}_j = H_j(x)\begin{bmatrix} \mathsf{A}_j \\ \mathsf{B}_j \\ \mathsf{C}_j \\ \mathsf{D}_j \end{bmatrix}, \tag{51}$$

where $H_j(x) = H^{(a)}H^{(b)}(x)$ and the index j means that we considered all the parameters of the j-th layer.

A similar set of equations is defined in a solid with the change of parameters defined in Eqs.(33)-(36) and with the additional term describing the possible supplied thermal power density, as given in Eq. (37). Eventually, the solutions are rewritten in matrix form as

$$\begin{bmatrix} \widetilde{p} \\ v \\ q \\ T \end{bmatrix}_j = H_j(x)\begin{bmatrix} \mathsf{A}_j \\ \mathsf{B}_j \\ \mathsf{C}_j \\ \mathsf{D}_j \end{bmatrix} + \begin{bmatrix} S_j'' \\ 0 \\ 0 \\ S_j' \end{bmatrix}, \tag{52}$$

where, as before, $H_j(x) = H^{(a)}H^{(b)}(x)$ and the index j means that we considered all the parameters of the j-th layer. Moreover, $S'_j = \frac{S_j}{i\omega\rho_j C_{Vj}}$ and $S''_j = \alpha_{Tj}B_j S'_j = \frac{\alpha_{Tj}B_j S_j}{i\omega\rho_j C_{Vj}}$. Here, S_j represents the thermal power density supplied to the j-th layer.

When all physical parameters of the layers are known, only the coefficients A_j, B_j, C_j, and D_j $\forall j$ are needed to fully determine the fields $\widetilde{p}$, v, q, and T everywhere in the system. In order to obtain a general procedure, we assume for each layer the solutions given by Eq. (52), which can be used for solid materials and also for fluid ones by simply letting $S_j = 0$.

3.2. Continuity conditions and general solution for the multilayered structure

The fields continuity between two layers can be written in matrix form as

$$H_j(l_j)\begin{bmatrix}\mathsf{A}_j\\ \mathsf{B}_j\\ \mathsf{C}_j\\ \mathsf{D}_j\end{bmatrix} + \begin{bmatrix}S''_j\\ 0\\ 0\\ S'_j\end{bmatrix} = H_{j+1}(l_j)\begin{bmatrix}\mathsf{A}_{j+1}\\ \mathsf{B}_{j+1}\\ \mathsf{C}_{j+1}\\ \mathsf{D}_{j+1}\end{bmatrix} + \begin{bmatrix}S''_{j+1}\\ 0\\ 0\\ S'_{j+1}\end{bmatrix}, \tag{53}$$

for $j = 1, \dots, N-1$. The fact that the first and the last layers are semi-infinite means that no progressive waves are considered for $j = 1$ and no regressive waves are considered for $j = N$. From the mathematical point of view, this can be written as $\mathsf{A}_1 = \mathsf{C}_1 = 0$ and $\mathsf{B}_N = \mathsf{D}_N = 0$. Moreover, we assume that no power density is supplied to the first and to the last layers of the structure, these regions being only subject to propagation. Using the fields continuity at each boundary between two layers, a relationship between B_1, D_1, A_N, and C_N is eventually found as

$$\begin{bmatrix}0\\ \mathsf{B}_1\\ 0\\ \mathsf{D}_1\end{bmatrix} = M_0\begin{bmatrix}\mathsf{A}_N\\ 0\\ \mathsf{C}_N\\ 0\end{bmatrix} + \sum_{n=2}^{N-1} M_{S_n}\begin{bmatrix}S''_n\\ 0\\ 0\\ S'_n\end{bmatrix}, \tag{54}$$

where n can span only over the layers with a non zero volumetric source and

$$M_0 = H_1^{-1}(l_1)\left[\prod_{j=2}^{N-1} H_j(l_{j-1})\,H_j^{-1}(l_j)\right]H_N(l_{N-1}), \tag{55}$$

$$M_{S_n} = H_1^{-1}(l_1)\left[\prod_{j=2}^{n-1} H_j(l_{j-1})H_j^{-1}(l_j)\right]\left[1 - H_n(l_{n-1})H_n^{-1}(l_n)\right]. \tag{56}$$

By means of Eq. (54) we can easily find A_N, C_N, B_1, and D_1. This allows the calculation of any coefficient (A_j, B_j, C_j, or D_j) using the expression ($\forall j = 1, \dots, N-1$)

$$\begin{bmatrix}\mathsf{A}_j\\ \mathsf{B}_j\\ \mathsf{C}_j\\ \mathsf{D}_j\end{bmatrix} = H_j^{-1}(l_j)\left\{H_{j+1}(l_j)\begin{bmatrix}\mathsf{A}_{j+1}\\ \mathsf{B}_{j+1}\\ \mathsf{C}_{j+1}\\ \mathsf{D}_{j+1}\end{bmatrix} + \begin{bmatrix}S''_{j+1}\\ 0\\ 0\\ S'_{j+1}\end{bmatrix} - \begin{bmatrix}S''_j\\ 0\\ 0\\ S'_j\end{bmatrix}\right\}, \tag{57}$$

if we start from the last layer and we calculate recursively the coefficients of the layers moving from the right to the left of the structure. Alternatively, we can use the relation ($\forall j = 2, \dots, N$)

$$\begin{bmatrix}\mathsf{A}_j\\ \mathsf{B}_j\\ \mathsf{C}_j\\ \mathsf{D}_j\end{bmatrix} = H_j^{-1}(l_{j-1})\left\{H_{j-1}(l_{j-1})\begin{bmatrix}\mathsf{A}_{j-1}\\ \mathsf{B}_{j-1}\\ \mathsf{C}_{j-1}\\ \mathsf{D}_{j-1}\end{bmatrix} + \begin{bmatrix}S''_{j-1}\\ 0\\ 0\\ S'_{j-1}\end{bmatrix} - \begin{bmatrix}S''_j\\ 0\\ 0\\ S'_j\end{bmatrix}\right\}, \tag{58}$$

if we start from the first layer and we calculate recursively the coefficients of the layers going from the left to the right of the structure. Finally, the main fields $\widetilde{p}$, v, q, T can be found for any x, within each layer, through Eq. (52).

4. Analysis and comparison with other models

In this Section, we take into consideration different configurations of thermophone devices and we analyze their frequency response by means of the previously introduced procedure. In addition, we compare our results with those of several models discussed in recent literature. The values of the physical parameters defining the materials (air, water, thermophone, solid

Table 1
Parameters describing the physical behavior of the materials constituting the thermophone systems investigated.

	ρ[kg · m^{-3}]	C_p[J · kg^{-1} · K^{-1}]	C_v[J · kg^{-1} · K^{-1}]	B[Pa]	α_T[K^{-1}]
Gas, air (g)	1.20	9.96×10^2	7.17×10^2	1.01×10^5	3.33×10^{-3}
Thermophone (s)	0.03×10^3	2.38×10^2	2.38×10^2	2.78×10^5	0.6×10^{-6}
Substrate (b)	4.5×10^3	5.23×10^2	5.23×10^2	1.14×10^7	9.00×10^{-6}
Fluid, water (w)	9.99×10^2	4.43×10^3	4.17×10^3	2.15×10^9	3.03×10^{-4}

Table 2
Other parameters describing the physical behavior of the materials constituting the thermophone systems investigated.

	λ[Pa · s]	μ[Pa · s]	λ_0[Pa]	μ_0[Pa]	κ[W · K^{-1} · m^{-1}]
Gas, air (g)	5.61×10^{-6}	1.68×10^{-5}	0	0	2.62×10^{-2}
Thermophone (s)	0	0	1.39×10^5	2.08×10^5	1.25
Substrate (b)	0	0	8.46×10^6	4.36×10^6	21.9
Fluid, water (w)	2.62×10^{-3}	1.14×10^{-3}	0	0	6.07×10^{-1}

substrate) used in this analysis are listed in Tables 1 and 2. The other parameters depend on the system investigated and can be found in Table 3. The most important quantity considered is the sound pressure level, which is defined by the following expression

$$\mathrm{SPL} = 20\log_{10}\left(\frac{p_{\mathrm{rms}}}{p_{\mathrm{ref}}}\right), \tag{59}$$

where p_{rms} is the root mean square pressure (i.e. $|p|/\sqrt{2}$, where p is the complex pressure introduced in previous sections) and p_{ref} is the reference sound pressure being, by definition, 20 μPa in air and 1 μPa in water.

It should also be noted that all plots show sound pressure level in the near field (NF) only. If some models from the literature have their equation in the far field (FF), they can be converted back in near field by using Rayleigh distance

$$R_0 = \frac{Af}{C_0}, \tag{60}$$

where A is the thermophone surface and $f = \frac{\omega}{2\pi}$ is the frequency. The approximation used is then

$$p_{\mathrm{FF}} = p_{\mathrm{NF}}\frac{R_0}{d}, \tag{61}$$

where d is the distance between the position of observation and the active surface of the thermophone.

4.1. Thermophone in free field

One of the most widely used model is the so-called *piston based model* introduced by Arnold and Crandall [2] and successively improved by Daschewski et al. [15] and Xiao et al. [14] by introducing effect of a substrate, the heat stored in the thermophone and the rate of heat loss per unit area of the device (due to conduction, convection, and radiation). This model considers the

Table 3
Specific geometrical parameters adopted in the analysis of different structures investigated. For each figure with SPL results, we clearly indicated the details defining the corresponding configuration. In all plots we assumed a thermophone surface $A = 4 \times 10^{-4}$ m^2 and an input power $P_{\mathrm{in}} = 1$ W. The rate of heat loss per unit area of thermophone β_s is considered only in Fig. 4 with the value $\beta_s = 28.9$ W/(m^{2}K). The viscosities λ and μ have been considered only in the results of Figs. 5 and 20.

	x[m]	L_b[m]	L_g[m]	L_s[m]
Fig. 3	$[5,10] \times 10^{-2}$	0	0	1×10^{-6}
Fig. 4	5×10^{-2}	0	0	1×10^{-6}
Fig. 5	5×10^{-2}	0	0	1×10^{-6}
Fig. 7	5×10^{-2}	∞	0	1×10^{-6}
Fig. 9	5×10^{-2}	1×10^{-5}	0	1×10^{-6}
Fig. 10	5×10^{-2}	∞	0	1×10^{-4}
Fig. 11	5×10^{-2}	∞	0	$[1,9,81] \times 10^{-6}$
Fig. 13	5×10^{-2}	$(1/27) \times 10^{-4}$	$(1/3) \times 10^{-4}$	1×10^{-6}
Fig. 14	5×10^{-2}	∞	8×10^{-4}	1×10^{-7}
Fig. 18	5×10^{-2}	0	$[0, 1/36, 1/12, 1/4, \infty] \times 10^{-4}$	1×10^{-6}
Fig. 20	5×10^{-2}	0	$[0, 1/10] \times 10^{-4}$	1×10^{-6}
Fig. 21	5×10^{-2}	0	$[1/16, 1/12, 1] \times 10^{-4}$	1×10^{-6}

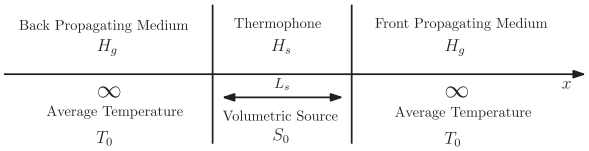

Fig. 2. Schematic of a thermophone radiating in free field. The plane waves are symmetrically generated within the back and the front media.

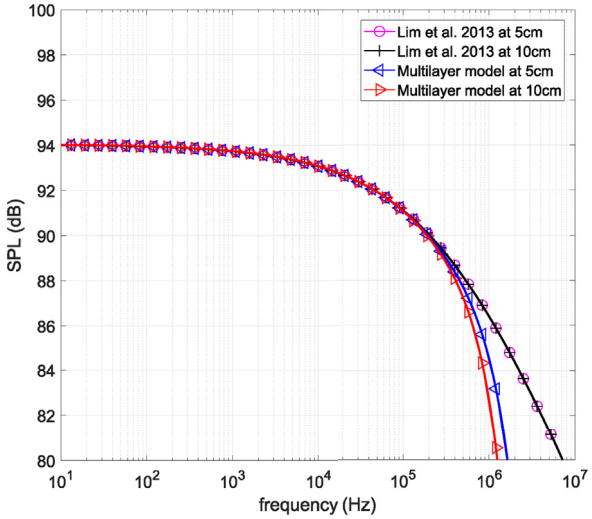

Fig. 3. Frequency response of the thermophone in free field determined by means of the Lim et al. model [25] and our multilayer model. We plotted here the results for $\beta_s = 0$ and for two different observation distances.

thermophone radiating in free field from both sides, as shown in Fig. 2. The sound generation is assumed to occur at the surfaces of the thermophone, in the so-called thermal layer, which is usually quite thin as specified in Eq. (23). In these models, the influence of the thermophone thickness L_s is considered through the HCPUA given by $C_s = \rho_s C_{p,s} L_s$. Lim et al. [25] also developed an improved model based on the previous assumptions but they described the thermoacoustic propagation with a real coupling between mechanical and thermal waves. In any case, since the order of magnitude of the acoustic wavenumber is much lower than the one of the thermal wavenumber, the results of Refs. [14,25] show good consistency. For comparison, the result of Lim et al. [25] is rewritten here as

$$p_{\mathrm{rms,NF}} = \frac{P_{\mathrm{in}}}{2\sqrt{2}A} \frac{\gamma_g - 1}{\left| \beta_s + \kappa_g \sqrt{\frac{\mathrm{i}\omega}{\alpha_g}} + \frac{1}{2}\mathrm{i}\omega C_s \right|} \sqrt{\frac{\omega}{\alpha_g}} \frac{\kappa_g}{C_0}, \tag{62}$$

where β_s is the rate of heat loss per unit area of thermophone (W/(m^{2}K)), which includes the influence of conduction, convection, and radiation. Moreover, C_s is the thermophone HCPUA, κ_g is the thermal conductivity, α_g is the thermal diffusivity $\frac{\kappa}{\rho C_p}$ and γ_g is the ratio C_p/C_v of the propagation region (gas). In addition, A is the thermophone area, P_{in} is the input power and, finally, C_0 is the isentropic sound velocity (NF stands for near field).

In Fig. 3 the result from Eq. (62) is compared to our model. Here, we adopted $\beta_s = 0$ and it can be seen that both models are consistent with each other from 1 Hz to about 100 kHz. The difference observed in high frequencies is explained by fact that Eq. (62) (and most literature models) uses a 0-th order approximation for the acoustic and thermal wavenumber, as explained in Section 2.1. If this approximation holds for a standard hearing frequency range (20–20 kHz), when considered at very high frequencies it gives inaccurate results since the first order (and higher) terms become not negligible and should be taken into consideration (see Eqs. (19) and (20) for details).

In our model, where we consider the exact thermal and acoustic wavenumbers, it is interesting to remark that the high frequency drop depends on the distance between thermophone and observation point. As a matter of fact, the drop will occur at lower frequencies as this distance is increasing, limiting the high frequency efficiency of the thermophone for large distances. This behavior can be only observed with an accurate determination of the wavenumbers, as observed in Fig. 3, where we plotted the frequency response at two different observation positions.

We further discuss the origin of the drop at high frequency, independently of the approximations adopted. As it is known, the sound generated by a thermophone occurs due to the fluctuation of heat in the air layer near the thermophone. The thickness

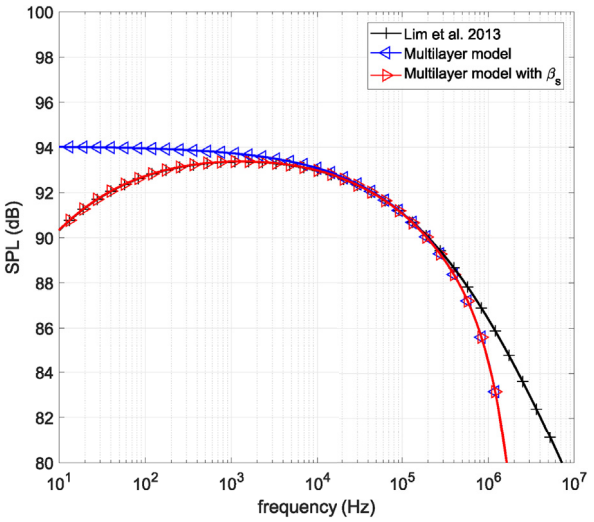

Fig. 4. Frequency response of the thermophone in free field determined by means of the Lim et al. model [25] and our multilayer model. We plotted here the results for $\beta_s = 28.9$ and we also shown the response obtained through the multilayer model with $\beta_s = 0$ for comparison.

of this active layer is related to the thermal wavenumber and is given by Eq. (23). It is then proportional to $1/\sqrt{\omega}$ whereas the acoustic wavelength is proportional to $1/\omega$. Since for low frequencies the thermal layer is much smaller than the acoustic wavelength, in this condition the sound is generated first in the thermal layer (a small fraction of the acoustic wavelength) and then propagated in the adjacent medium. This however stops to be true for high frequencies due to the different decreasing rate of each wavelength. We explain the behavior when the thermal layer is larger than the acoustic wavelength as follows. In this case, many acoustic wavelengths compose the thermal layer. Since the thermal wavelength is of the same order of the thermal layer, the spatial temperature variations (slower) are not able to follow the spatial pressure variation (faster) and the sound generation becomes less efficient, thus generating the observed drop in Fig. 3 (both models).

Fig. 4 shows the results for the same configuration of Fig. 3 but now with a non zero coefficient β_s, taking into account the rate of heat loss per unit area of thermophone. It is seen that the mid and high frequency range doesn't change but at low frequencies there is a drop in the SPL. The heat loss has been implemented rigorously also in our model, by suitably modifying the continuity equation for the heat flux. In particular, this continuity equation have been readdressed for the two interfaces of the system, which can be seen in Fig. 2. The updated flux balance at the interfaces can be written as

$$-\beta_s T(l_1) - \kappa_1 \frac{\mathrm{d}T}{\mathrm{d}x}(l_1) = -\kappa_2 \frac{\mathrm{d}T}{\mathrm{d}x}(l_2), \tag{63}$$

$$-\kappa_2 \frac{\mathrm{d}T}{\mathrm{d}x}(l_2) = -\kappa_3 \frac{\mathrm{d}T}{\mathrm{d}x}(l_2) + \beta_s T(l_2), \tag{64}$$

where β_s quantifies the heat loss, which is considered proportional to the temperature. While this is a good approximation for losses due to conduction and convection, it is however a poor representation of the radiated heat, which is typically proportional to the fourth power of the temperature. Here, we also have $l_1 = 0$ and $l_2 = L_s$ to be coherent with Fig. 2. Papers which take β_s into account determined its value through experimental results [14,18,25]. The good agreement between our modified model and results from Lim et al. [25] is clearly shown in Fig. 4.

Lastly, Fig. 5 displays the results of our model with and without the air viscosity. It is seen that adding viscosity increases the high frequency drop rate. Since its influence is negligible for frequencies lower than 100 kHz, the literature models often neglect it (except for Refs. [15,16]).

4.2. Thermophone on substrate

Another important structure investigated in the literature consists in a thermophone layer directly placed on a substrate (without gap) and radiating in air, as shown in Fig. 6. One model describing this system has been developed by Hu et al. [20]. This model is based on the balance equations earlier developed for describing the photoacoustic effect [19], and aims at reproducing the experimental results presented by Shinoda et al. [5]. This model takes the thickness of the thermophone into account and consider the conservation of energy in the solids but neglect the propagation of the acoustic wave inside it. By using a surface input power P_{in}/A, the obtained pressure is [20]

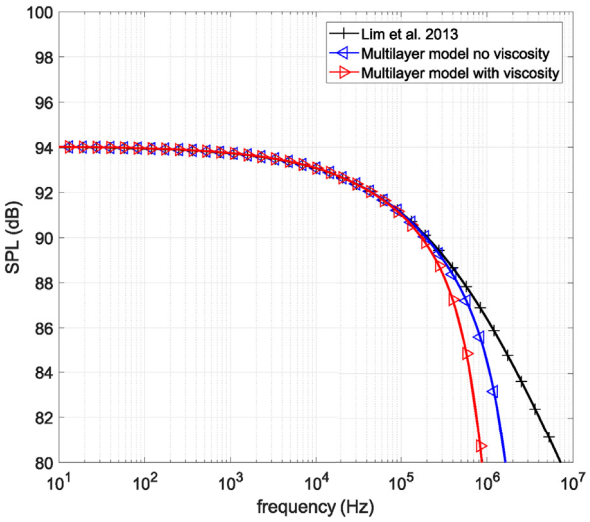

Fig. 5. Frequency response of the thermophone in free field determined by means of the Lim et al. model [25] and our multilayer model. We plotted here the results for $\beta_s = 0$ at a distance of 5 cm, and we introduced the air viscosity in our model to show its effect at high frequency.

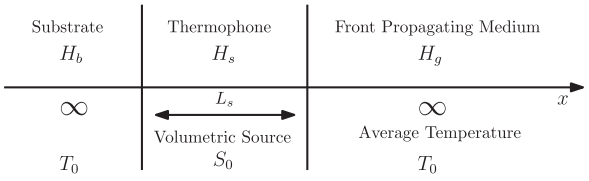

Fig. 6. Schematic of a thermophone placed on a solid substrate on the left and radiating in free field on the right. The plane waves are non-symmetrically generated within the back and the front media.

$$p_{\mathrm{rms,NF}} = \left| \frac{\mathrm{i}d_t d_a k_g}{\mathrm{i}d_a k_g(M\kappa_s\sigma_s + \kappa_g\sigma_g) - d_t\sigma_g(M\kappa_s\sigma_s + \mathrm{i}\kappa_g k_g)} \left(\mathrm{e}^{-\sigma_g x} - \frac{\sigma_g}{\mathrm{i}k_g}\mathrm{e}^{-\mathrm{i}k_g x} \right) \frac{P_{\mathrm{in}}}{A\sqrt{2}} \right|. \tag{65}$$

The use of a surface density power (instead of a volume density power as in other theories and in our model) is justified by the fact that this model is dedicated to the Shinoda et al. experiment, in which there is a 30 nm aluminum film acting as the heat source. Most models are however considering that the whole thermophone is heating and so it is interesting to see how Hu's model holds with a volumetric source. By replacing the surface input power P_{in}/A with a volumetric source $\frac{P_{\mathrm{in}}}{AL_s}\frac{1}{\mathrm{i}\omega\rho_g C_{p,g}}$ and using the same assumptions of Hu's model, we obtained the volumetric counterpart of Eq. (65), as follows

$$\begin{aligned} p_{\mathrm{rms,NF}} = \Bigg| & \frac{1}{\mathrm{i}\omega L_s \rho_g C_{p,g}} \frac{\kappa_s\sigma_s}{\kappa_s\sigma_s - \kappa_b\sigma_b} \left(\mathrm{e}^{\sigma_s L_s}\kappa_b\sigma_b(M-1) + M(\kappa_s\sigma_s - \kappa_b\sigma_b) \right) \\ & \times \frac{\mathrm{i}d_t d_a k_g}{\mathrm{i}d_a k_g(M\kappa_s\sigma_s + \kappa_g\sigma_g) - d_t\sigma_g(M\kappa_s\sigma_s + \mathrm{i}\kappa_g k_g)} \left(\mathrm{e}^{-\sigma_g x} - \frac{\sigma_g}{\mathrm{i}k_g}\mathrm{e}^{-\mathrm{i}k_g x} \right) \frac{P_{\mathrm{in}}}{A\sqrt{2}} \Bigg|. \end{aligned} \tag{66}$$

In Eqs. (65) and (66) the following definitions have been introduced following Ref. [20].

$$M = \frac{(\kappa_b\sigma_b + \kappa_s\sigma_s)\mathrm{e}^{\sigma_s L_s} + (\kappa_b\sigma_b - \kappa_s\sigma_s)\mathrm{e}^{-\sigma_s L_s}}{(\kappa_b\sigma_b + \kappa_s\sigma_s)\mathrm{e}^{\sigma_s L_s} - (\kappa_b\sigma_b - \kappa_s\sigma_s)\mathrm{e}^{-\sigma_s L_s}}, \tag{67}$$

$$d_t = \frac{\mathrm{i}\omega\kappa_g - \sigma_g^2\alpha_g\kappa_g}{\mathrm{i}\omega\alpha_g}, \tag{68}$$

$$d_a = \frac{\mathrm{i}\omega\kappa_g + k_g^2\alpha_g\kappa_g}{\mathrm{i}\omega\alpha_g}. \tag{69}$$

Here, the coefficients k and σ are the acoustic wavenumber and the thermal attenuation of each layer.

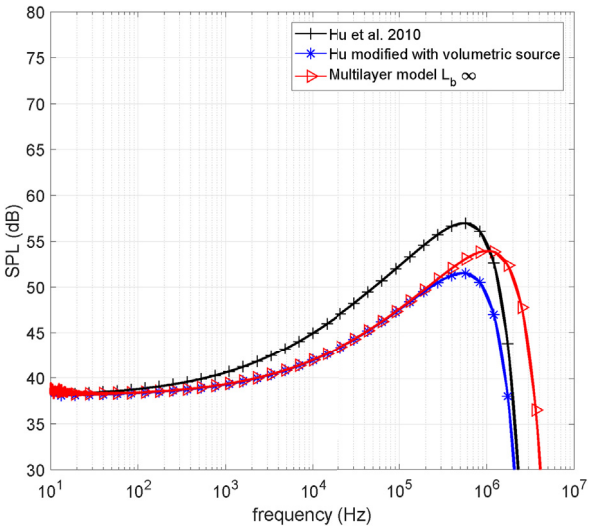

Fig. 7. Frequency response of a thermophone in contact with a semi-infinite substrate on the left and propagating in air on the right (see the scheme in Fig. 6). We compare the result of our multilayer model with Eq. (65) [20] and Eq. (66).

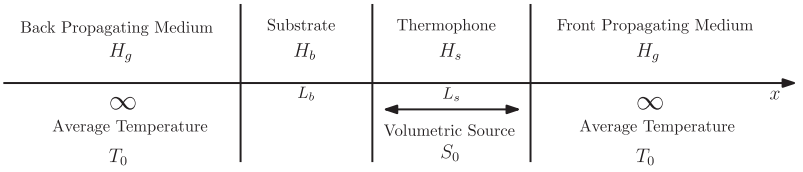

Fig. 8. Schematic of a thermophone placed on a solid substrate of finite thickness on the left, and radiating in free field on the right. The plane waves are non-symmetrically generated within the back and the front media.

The comparison of Eqs. (65) and (66) with our model, where we used a semi-infinite substrate as shown in Fig. 6, can be found in Fig. 7. It can be seen that there is a perfect match between Eq. (66) and our model for low and mid frequencies. For frequencies above 200 kHz there is a discrepancy between the volumetric source version of Hu's model and our model. This is due to a difference in the acoustic wavenumber first order approximation. As a matter of fact, Eqs. (19) and (20) differ slightly with Hu's solutions and this is only significant at very high frequencies. Indeed, if the wavenumbers used by Hu et al. are introduced in our model, there is a perfect agreement also at high frequencies. On the other hand, the case with a surface input power, described by Eq. (65), shows a higher SPL in the whole frequency range, as expected since there is no heat stored in the thermophone.

We consider now the case with a finite thickness of the substrate, as shown in Fig. 8. This more elaborated structure can be studied through our multilayer model, and in Fig. 9 a rise of SPL in the low frequency domain can be seen. In general, the presence of the substrate is useful for technological reasons, but it absorbs a large amount of heat and reduces therefore the thermophone output SPL, as seen in Fig. 7. However, a small thickness of the substrate may help to ameliorate the performance. The observed SPL rise is due to the fact that since for lower frequencies the thermal penetration depth is larger, when the substrate is of a comparable order of magnitude, it will absorb less heat and so the thermophone is more efficient. The lower the frequency, the less impact the substrate has on the radiation and so the sound pressure may attain a free field radiation level. A more detailed analysis of the heat flux lost in the substrate can be found in Ref. [39].

To further investigate this configuration, we come back to the structure with infinite substrate shown in Fig. 6, and we investigate the influence of the size of the thermophone. In Fig. 10, we plotted our results with Eq. (62) (free field model), and with Eqs. (65) and (66). In this analysis, the thermophone is a hundred time thicker than before. First, it can be seen that the Hu et al. [20] model with a surface input power displays a significant rise in SPL. This rise is proportional to the thickness of the thermophone and is explained by the parameter M in Eq. (65). It approaches the value 1 for a surface input power, generating a flat frequency response in a given interval, as discussed in Ref. [20]. Indeed, concentrating the input power at the thermophone surface is more efficient than distributing the same power over the whole thermophone body, as already seen in Figs. 7 and 9.

We consider now the case with a volumetric input power. Fig. 10 displays that the model with a substrate is consistent with the decreasing response of the free field model for frequencies higher than 10 kHz. This decreasing behavior is due to the rise of HCPUA and, therefore, to the heat stored in the sample. The fit between free field and substrate model is due to the size of

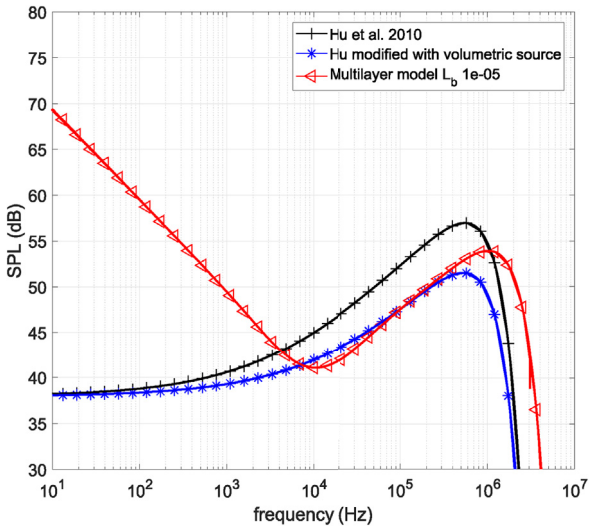

Fig. 9. Frequency response of a thermophone placed on a substrate with finite thickness and radiating in air (see scheme in Fig. 8). We compare the result of our multilayer model with Eq. (65) [20] and Eq. (66).

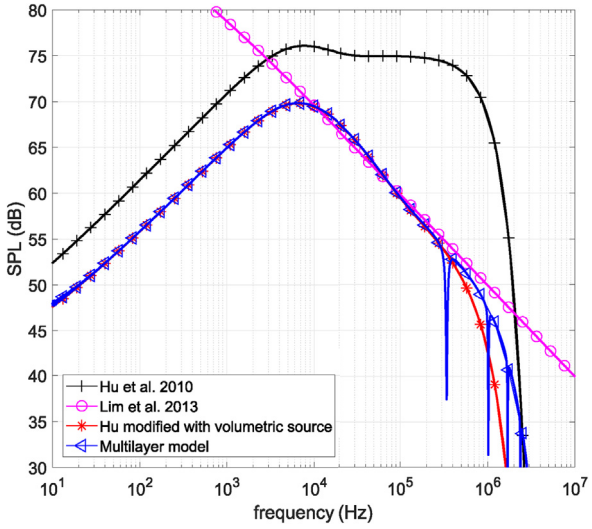

Fig. 10. Frequency response of a thermophone in contact with a semi-infinite substrate on the left and propagating in air on the right (see the scheme in Fig. 6). The thermophone is here a hundred time thicker than in previous plots. We compare the result of our multilayer model with Eq. (62) by Lim et al. [25], Eq. (65) by Hu et al. [20] and Eq. (66) (modification with volumetric source).

the thermophone that is larger than the thermal penetration depth, thus leading to negligible influence of the substrate. It is interesting to show how the SPL of the system with increasing thermophone thickness changes moving from the case of Fig. 7 to the one of Fig. 10. This response evolution can be found in Fig. 11, where three increasing values of L_s are considered and the results of our model are compared with Eq. (62), holding for the free field model. It is interesting to note that for increasing L_s the response of the multilayer model approaches asymptotically the response of the free field model, confirming the above discussion.

Lastly, anti-resonances around 1 MHz can be seen in our model (Figs. 10 and 11). These are mechanical anti-resonances occurring in the thermophone structure that can be analyzed through our model since we solve the complete set of wave equations in the solid layer. If these resonances/anti-resonance were mentioned in Brown et al. [29], they were never estimated before since they were supposed to occur at a frequency higher than the range of interest. These resonances can be attenuated by increasing the viscosity of the solid, and are influenced by the Young modulus of the thermophone as well.

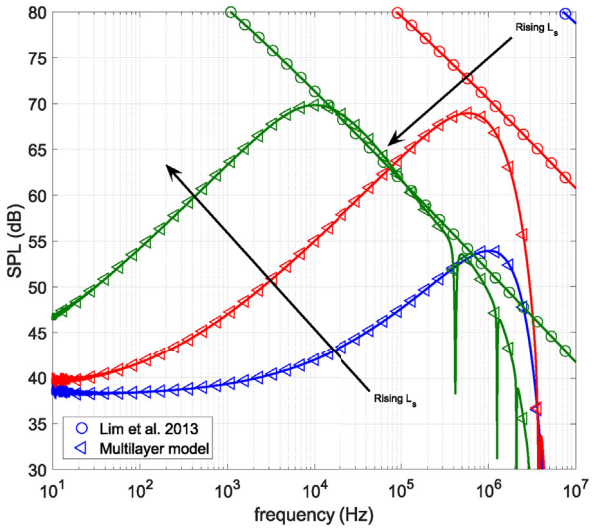

Fig. 11. Frequency response of a thermophone with increasing thickness L_s in contact with a semi-infinite substrate on the left and propagating in air on the right (see the scheme in Fig. 6). We compare the results of our multilayer model with Eq. (62), describing the free field thermophone [25].

4.3. Thermophone over a substrate with air gap

The most complicated structure investigated in the literature is obtained by adding a small air gap between the thermophone and the substrate, as shown in Fig. 12. This kind of design was investigated by Vesterinen et al. [28] and by Tong et al. [26], in continuity with the free field modeling by Lim et al. [25]. Both articles consider the classical balance equations and the Tong's model also takes the heat loss into account. These models however do not consider explicitly the thermophone solid layer, which is implicitly described by the HCPUA factor. As a result of their calculations, assuming that there is a perfect sound reflection from the backing, Vesterinen et al. [28] determined an absolute maximum value for the sound pressure level of a thermophone as

$$p_{\mathrm{rms,NF,max}} = \frac{P_{\mathrm{in}} C_0}{\sqrt{2} A C_{p,g} T_0}. \tag{70}$$

Eq. (70) shows that the maximum sound pressure achievable for a given thermophone will only depend on the properties of the propagating medium. The input power or the ambient temperature can also be independently optimized. In order to see if this maximum pressure is achievable, an air gap between the thermophone and the substrate is added to our model and the results are compared with Tong's equation [26].

$$p_{\mathrm{rms,NF}} = \left| \frac{C_0}{T_0 C_{p,g}} \frac{\overline{P_{\mathrm{in}}}}{2\sqrt{2}A} \left[(\mathbf{R}-1)\mathrm{e}^{-\sigma_g L_g} + \mathrm{e}^{-\mathrm{i}k_g L_g} + 1 \right] \mathrm{e}^{-\mathrm{i}k_g x} \right|, \tag{71}$$

where

$$\overline{P_{\mathrm{in}}} = \frac{-\sigma_g \kappa_g P_{\mathrm{in}}}{(2\beta_s + \mathrm{i}\omega C_s)(1 + \mathbf{R}e^{-2\sigma_g L_g}) + 2\sigma_g \kappa_g}, \tag{72}$$

and

$$\mathbf{R} = \frac{\sqrt{\alpha_g} - \sqrt{\alpha_b}}{\sqrt{\alpha_g} + \sqrt{\alpha_b}} \tag{73}$$

is the reflection coefficient of the thermal wave.

Fig. 13 displays the comparison among our model, the Tong model, the Lim free field model and the Vesterinen maximal value. Here, the substrate is of finite size and the air gap is 0.033 mm wide. It is seen that at low frequencies there is a large difference between Tong's model and ours. In the mid range frequency there is good consistency between the models, and these results are close to the Vesterinen upper bound. Then, at high frequency, we observe a drop, which starts sooner in our model for the same reasons already explained in Section 4.1. The low frequency differences are due to the fact that the substrate has a finite size in our model and therefore is not as reflective as it is in Tong's model. It is important to remark that in the frequency range between 10 KHz and 1 MHz, the thermophone response is much larger than the free field level represented by the Lim et al. [25] result and exhibits a peak which is close to the Vesterinen upper bound. This behavior is due to the size of the air

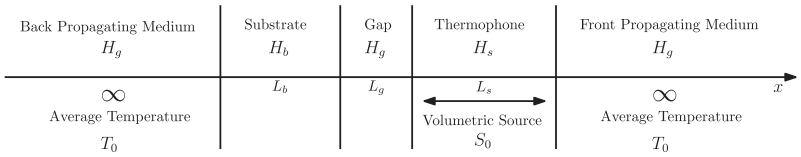

Fig. 12. Schematic of a thermophone placed on a solid substrate of finite thickness on the left, and radiating in free field on the right. The plane waves are non-symmetrically generated within the back and the front media.

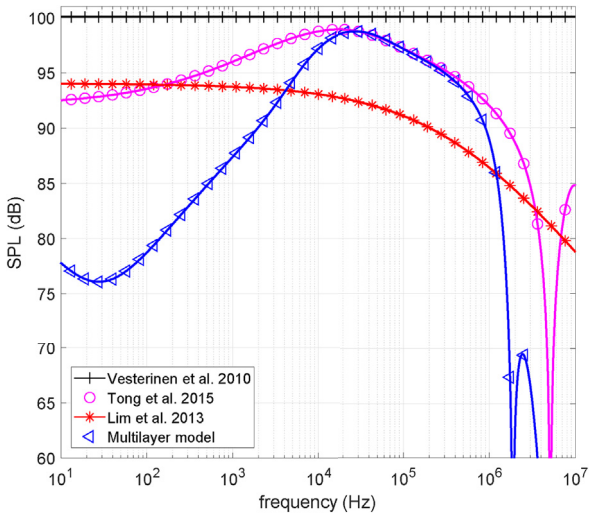

Fig. 13. Frequency response of a thermophone placed over a substrate with an air gap, as shown in Fig. 12. The result of the multilayer model can be compared with Eq. (71) (Tong et al. [26]). Moreover, we reported the result of the free field model given in Eq. (62) (Lim et al. [25]) and the Vesterinen et al. [28] upper bound reported in Eq. (70).

gap between thermophone and substrate. Indeed, we know that the thermal layer (in which the sound is generated) is larger for low frequencies than for high frequencies. Hence, if the air gap is not large enough, there will be heat loss in the substrate eventually leading to poorer SPL than in free field, as seen for frequencies below 1.5 KHz. On the other hand, for frequencies generating a thermal layer similar to or smaller than the air gap, we have no heat loss in the substrate and it simply acts as a reflector, doubling the sound pressure, or equivalently, adding $20\log_{10}(2) = 6$ dB to the SPL. This intensification can be seen above 10 KHz. Furthermore, above 1 MHz our model and the Tong's model display air gap anti-resonances leading to poorer SPL around these frequencies. These resonances occur before any mechanical resonance or anti-resonance within the thermophone layer and therefore they are more critical for the thermophone system design.

In Fig. 14 the substrate is now infinitely large in our model and the air gap size is more than ten times larger ($L_g = 0.8$ mm). It is seen that from 200 Hz to 10 kHz there is less than 1 dB difference between Vesterinen maximum SPL and Tong's model or ours. In this region, compared to the free field model, there is a 6 dB improvement, which is consistent with a regular sound source with double sound pressure due to the backing reflection. Indeed, in this configuration the air gap is much larger than the thermal layer in the whole range from 200 Hz to 10 KHz and we have no heat loss in the substrate. It can be noticed that around 50 Hz the results are above Vesterinen upper limit. This can be explained by the specific parameters acting as a second order filter with a typical underdamped response. The low frequency differences between Tong result and ours in Fig. 14 are still due to a non perfect reflection from the substrate even though the infinite size improved it. To conclude, depending on the frequency range in which the thermophone is supposed to work, it is important to determine whether the air gap is useful to improve the sound pressure level compared to free field emission.

5. Comparison with experiments

In this Section, in order to validate the model against real measurements, we compare the results of our approach with some recent experimental investigations [40,41].

The first measurements concern the comparison between carbon multi-walled nanotubes (MWNT), providing the most attractive performance as thermoacoustic generator, and an alternative solution given by poly-acrylonitrile nanofibers (PAN) coated by indium-tin oxide (ITO) [40]. Indeed, the limited accessibility to large-size carbon MWNT sheets has promoted the research for alternative materials with interesting performances. In Fig. 15 one can find the experimental results and the theo-

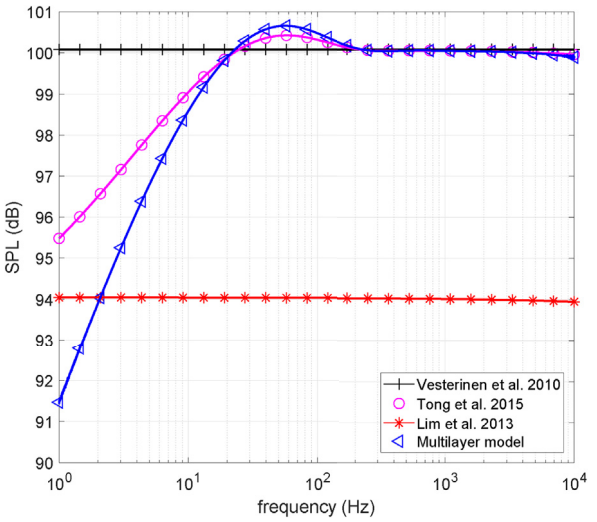

Fig. 14. The same plots of Fig. 13 for a structure shown in Fig. 12, where the substrate is now infinitely large and the air gap size is more than ten times larger. In this case, our result and the Tong's model [26] achieve the SPL upper bound predicted by Vesterinen [28], corresponding to a 6 dB improvement with respect to the Lim's free field model [25].

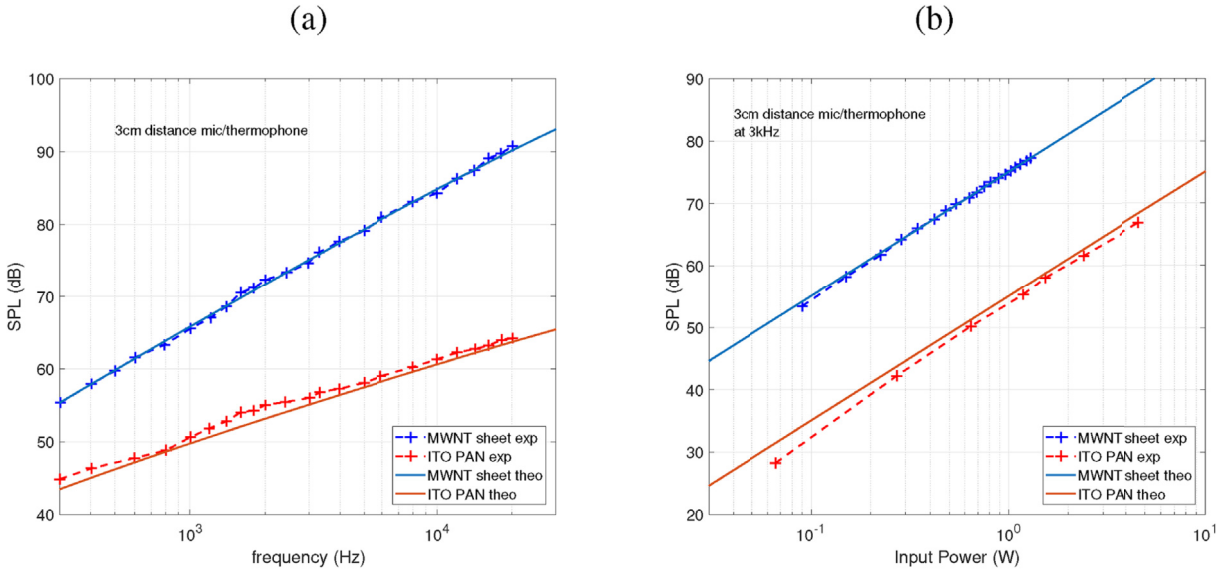

Fig. 15. Comparison between the thermoacoustic performances of carbon MWNT sheets and ITO-PAN sheets (experimental and theoretical results). Panel (a): frequency response of the two materials showing the behaviors SPL $\sim f^{1.0}$ for MWNT and SPL $\sim f^{0.53}$ for ITO-PAN (the plots correspond to a normalized power of 1 W). Panel (b): SPL versus input power for the two materials.

retical ones. The curves for the single-layer MWNT sheet correspond to a sample with surface 1.5×1.5 cm^2 and with an applied power of $P_{\text{in}} = 0.24$ W. On the other hand, the curves for the both-sides ITO-coated PAN sheet correspond to a sample with surface 1.2×1.5 cm^2 and with an applied power of $P_{\text{in}} = 0.29$ W. Both experimental results have been obtained at a distance of 3 cm from the thermophone surface [40]. We remark that the frequency responses shown in Fig. 15 have been normalized for an input power of 1 W, in order to facilitate the comparison between the material performances.

The theoretical results shown in Fig. 15 have been obtained with the free field model described in Section 4.1, where we introduced all the physical parameters given in Ref. [40]. For both the frequency response and the behavior of the SPL versus the input power, we observe a very good agreement between theory and experiments. Concerning the frequency response, the capacity of the model to represent the two different slopes SPL $\sim f^{1.0}$ for MWNT and SPL $\sim f^{0.53}$ for ITO-PAN proves that our approach is able to work with a HCPUA varying over several order of magnitude. Indeed, we have that HCPUA $= 13 \times 10^{-3}$ Jm^{-2}K for single-layer MWNT sheets and HCPUA $= 0.67$ Jm^{-2}K for ITO-coated PAN sheets. These values can be determined by observing that $\rho_s = 1$ kg/m^3, $C_{p,s} = 716$ JKg^{-1}K^{-1}, $L_s = 18 \times 10^{-6}$ m for the MWNT sheet and

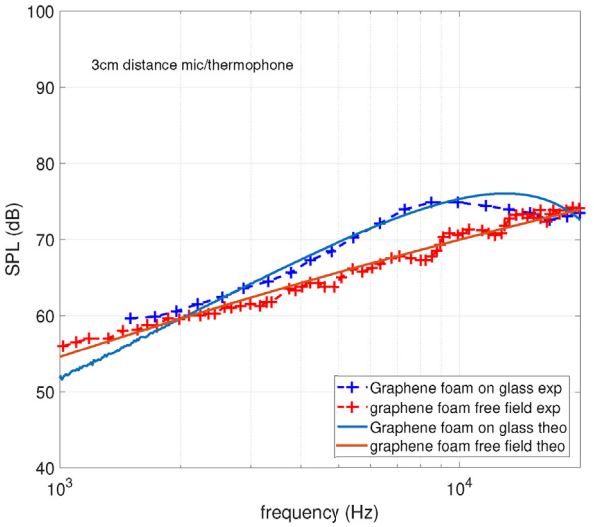

Fig. 16. Experimental and theoretical frequency responses of FDGF thermophones. Both the free field case and the geometry with substrate have been considered. The free field case is well described by the relation SPL $\sim f^{0.75}$, which can be compared with MWNT and ITO-PAN thermophones shown in Fig. 15.

$\rho_s = 220\ \mathrm{kg/m^3}$, $C_{p,s} = 606\ \mathrm{JKg^{-1}K^{-1}}$, $L_s = 5 \times 10^{-6}$ m for the ITO-PAN sheets [40]. In addition, the linearity of the SPL-versus-power curves shows the linear behavior of the acoustic response in terms of the applied electric power, as implemented in the model.

We remark that the measurements presented in Fig. 15 concern the acoustic far field response of the thermophone (distance of 3 cm from a thermophone with area $1.5 \times 1.5\ \mathrm{cm^2}$ or $1.2 \times 1.5\ \mathrm{cm^2}$). Therefore, in order to compare these far field measurements with our near field theoretical results, we have numerically implemented an acoustic diffraction calculation. For a planar surface at $x = x_0$ vibrating with the velocity $v(y,z)$, each point can be considered as an acoustic source. Therefore, the actual pressure field can be found by superposition, using Rayleigh's second integral

$$p_{\mathrm{FF}}(x,y,z) = \frac{\mathrm{i}\omega\rho_g}{4\pi}\int_{-L_y}^{L_y}\int_{-L_z}^{L_z} v(y',z')\frac{e^{-\mathrm{i}k_g\sqrt{(x-x_0)^2+(y-y')^2+(z-z')^2}}}{\sqrt{(x-x_0)^2+(y-y')^2+(z-z')^2}}dz'dy', \tag{74}$$

where x, y and z are the coordinates of the observation point and x_0, y' and z' those of the generation point. The rectangle $(-L_y, L_y) \times (-L_z, L_z)$ of the plane represents the vibrating region. Here, we introduced the factor 4π in the denominator of the expression since we considered any point source radiating in free field and not attached on a substrate. In order to use Eq. (74), we considered the velocity field in air, calculated through our near field model, for a distance from the thermophone slightly larger than the thickness of the thermal layer (active region). Indeed, at this distance, the velocity has attained its maximum value, which can be considered for the acoustic propagation in Eq. (74). The thickness of the thermal layer has been evaluated through the approximated expression $\mathcal{L}_{th} = 2\sqrt{\frac{C_0 l_k}{2\omega\gamma}} = \sqrt{\frac{2\alpha}{\omega}}$ (see Section 2.1). Hence, the theoretical curves in Fig. 15 represents the results of the Rayleigh's second integral applied to the velocity field of our near field model. In other words, our multilayer model is used to describe the thermoacoustic generation of waves (which is mostly wideband, as discussed in Section 4.1), whereas the diffraction theory is used to properly take into account the resulting acoustic propagation.

A second comparison with experimental measurements can be found in Fig. 16. In this case we considered the results for the freeze drying graphene foam (FDGF) thermophone discussed in Ref. [41]. The FDGFs are particular graphene foams obtained with a specific procedure implemented to get uncollapsed structures, which are more efficient from the thermoacoustic point of view [41]. This material has been used as thermophone in free field and as thermophone located on a glass substrate (with a small gap). The acoustic measurements have been performed at a distance of 3 cm for an applied power of 0.1 W. In Fig. 16, one can find the experimental and theoretical results for both the free field thermophone and the system with a glass substrate. Again, we can observe a quite good agreement between theory and experiments. For the case of the thermophone located on the substrate we supposed a gap of 1 μm between FDGF and glass and we used the theory introduced in Section 4.3. For the implementation of the model we used the parameters declared in Ref. [41]. It is interesting to observe that the slope of the frequency response is accurately described by the expression SPL $\sim f^{0.75}$, representing an acoustic performance in-between single-layer MWNT sheets and ITO-coated PAN sheets, previously introduced. As a matter of fact, this slope corresponds to a HCPUA of 0.2 $\mathrm{Jm^{-2}K}$, which is a value between 0.013 $\mathrm{Jm^{-2}K}$ and 0.67 $\mathrm{Jm^{-2}K}$, corresponding to MWNT and ITO-PAN, respectively. To conclude, also the theoretical curves in Fig. 16 have been obtained by combining the Rayleigh diffraction calculation with our near field model, as previously discussed.

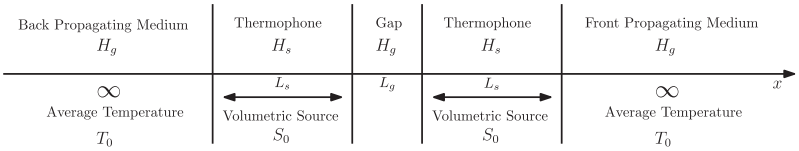

Fig. 17. Schematic of a sound generation system composed of two thermophone layers placed in air, separated by an air gap, and radiating symmetrically in both directions.

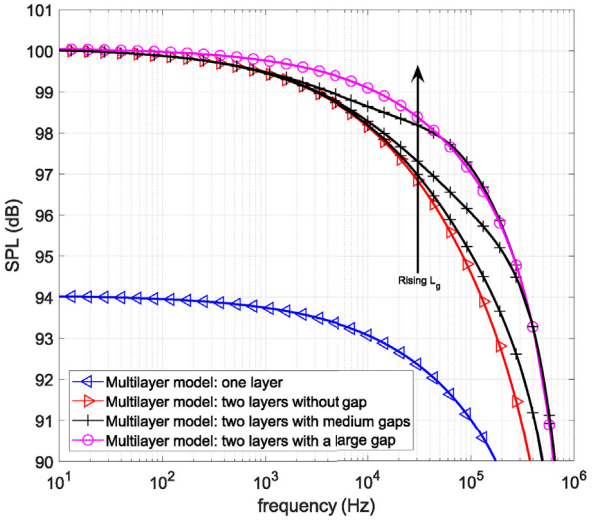

Fig. 18. Frequency response of a thermophone system composed of two generating layers separated by a given air gap (see Fig. 17 for details). We considered the case without gap $L_g = 0$, the case with medium gaps $L_g = 1/36, 1/12, 1/4 \times 10^{-4}$ m, and the case with a large gap $L_g = 1 \times 10^{-4}$ m (independent non-interacting layers). We can observe the effect of the air gap width and compare the result with the single layer thermophone system.

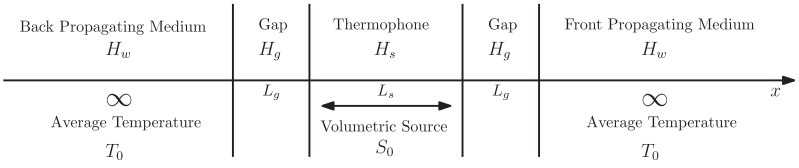

Fig. 19. Schematic of a thermophone placed in water by means of two symmetric air gaps, and radiating symmetrically in both directions.

6. Analysis of novel thermophone systems

Two new configurations will now be studied using the multilayer model. The first case consists in a thermophone with (two or more) parallels generating layers, separated with air gaps. A simple case with only two generating layers, as seen in Fig. 17, will be investigated by considering a fixed input power densities and the same thickness of both layers. The influence of the width of the air gap between the layers will then be examined, discussed and compared to the results of Aliev et al. [6] and those of Barnard et al. [7].

The second case will concern the sound generation in an underwater environment. The response of a one layer thermophone in an underwater free field geometry will be compared to the free field response in air. Afterward, based on an interpretation made by Aliev et al. [30], an hydrophobic behavior of the thermophone layer will be considered, where an air gap is assumed between the thermophone and the water, as shown in Fig. 19. The results will be compared also with the Tong et al. theoretical model for encapsulated thermophones [31].

6.1. Multi generating layer thermophone

We analyze here the behavior of the system with two generating layers radiating symmetrically in air, as shown in Fig. 17. Fig. 18 displays the sound pressure level for two generating layers (each with thickness L_S and input power P_{in}), separated by an air gap of length L_g. For the sake of comparison, the free field response for a single generating layer is also plotted (with

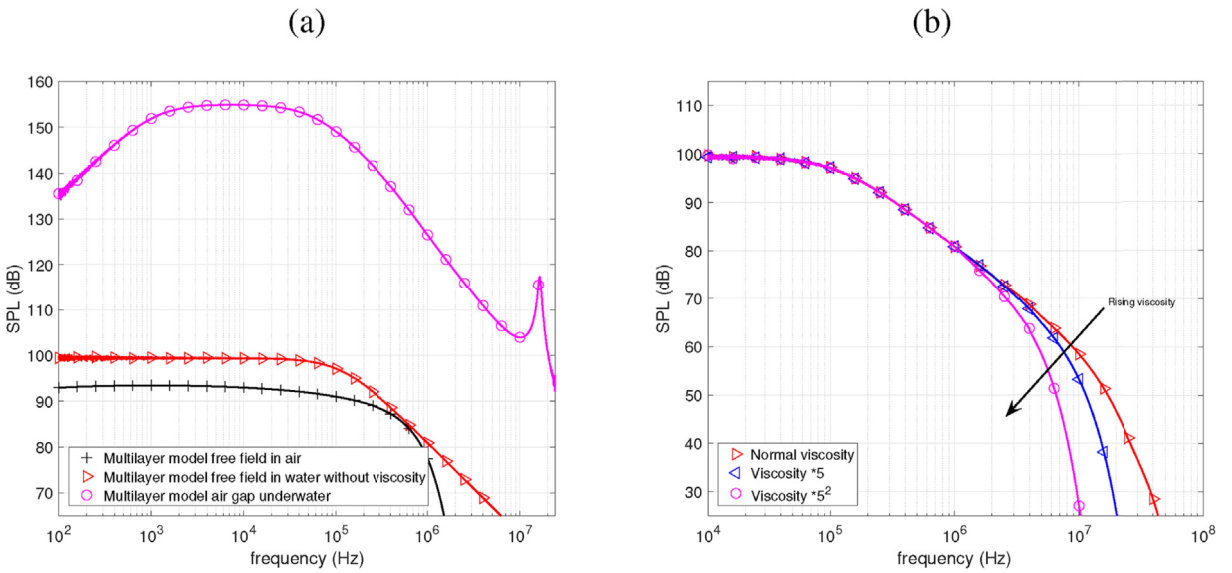

Fig. 20. Frequency response of a thermophone working underwater. Panel (a): we can compare the response of the underwater thermophone in free field without viscosity, the underwater thermophone with air gap (e.g. due to hydrophobicity as observed for carbon nanotubes), and finally, the thermophone working in air and in free field. Panel (b): response of the free field thermophone with the normal viscosity of water and two larger values of viscosity.

L_S and P_{in}). It is seen that for low frequencies there is a 6 dB rise in sound pressure level regardless of the distance between the thermophone layers. This rise is justified by the fact that the pressure generated by two similar layers leads to double the pressure if the signals are in phase and if they can propagate without obstacles. It means that the samples are still close enough to prevent any effect of the phase difference between the sound generated by each layer and that they are acoustically transparent to one another. Furthermore, it could have been expected to see a drop in the low frequency region when the air gap is of the same order of magnitude as the thermal layer. Since the gap length does not influence this low frequency region, we deduce that there is no heat interference due to the thermal layers between each generator.

In the mid to high frequency region it is seen that the sound pressure region drops faster with a smaller gap length. The small and large gap curves are limiting cases which can be reproduced by adapting the free field model. For instance, if $L_g \to 0$, then the double layer system gets similar to a single layer with $2L_s$ and $2P_{\text{in}}$. This does not change the input power density S_0 but, since the thermophone is larger, the HCPUA gets larger and the high frequency drop is more significant. On the other hand, if the gap is large enough to cancel the thermal capacity interaction between the layers but still small enough to not create any significant phase difference, then the acoustic response is similar to that of a single layer thermophone with twice the input power (i.e., with L_s and $2P_{\text{in}}$).

The observed rise in the SPL with a multi layer thermophone concurs with the findings of Barnard et al. [7] and Aliev et al. [6]; however, to complete this picture, we added here the analysis of the influence of the air gap size. Although the same SPL level of this structure can be easily reproduced with a single layer thermophone by changing the input power, there is an important reason to adopt this double configuration. As explained by Aliev et al. [6], the maximum power density supplied to the thermophone must be limited to avoid the material failure. Of course, the simplest solution to improve the SPL without lowering the HCPUA is to increase the input power. However, the increase of the power density may generate material failure. Furthermore, the improvement of HCPUA is typically limited by the technological procedures adopted. Then, for a fixed thermophone geometry with a limited power density before failure, an interesting solution to improve the SPL is to use a multilayer geometry.

6.2. Underwater thermophone systems

The first investigations concerning underwater thermophone systems considered the encapsulation of the thermophone in a gas cavity [30–32]. This solution is useful to preserve the integrity of the thermophone material. However, the encapsulation can create resonances and therefore can limit the wide band frequency response. Consequently, this configuration will not be investigated here since we prefer to analyze systems with a possibly wide band frequency response. Firstly, we study the emission of a simple thermophone in a free field underwater configuration. Then, we examine the underwater thermophone with two air layers generated by the hydrophobic behavior of the thermophone material.

Fig. 20 displays the free field response of the thermophone with and without viscosity in water, with viscosity in air, and the results of an hydrophobic model. We remember that in water the SPL is calculated with a pressure reference of 1 μPa.

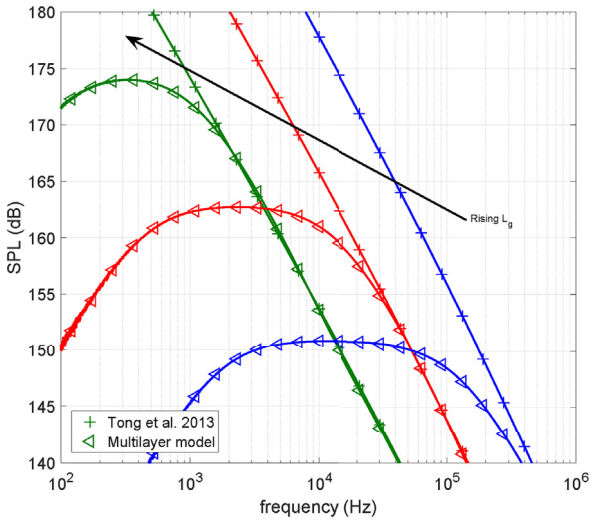

Fig. 21. Frequency response for the underwater thermophone with symmetric air gaps. We can find the responses for three different air gap widths and we compare our results with those of Eq. (75), proposed by Tong et al. [31]. We underline the good agreement for the high-frequency behavior.

The low frequency behavior corresponds to a flat response for both air and water. On the other hand, the high frequency decrease starts at a lower frequency in the water and has a different slope rate (20 dB/dec, see Fig. 20(a)). Those differences are mainly due to the change of parameters and reference pressure of the propagation medium. The individual parameters influence has not been further investigated here since other works have already done it considering various gases as propagation medium [31,33]. The free field response in air is reported here mostly for reference. We now look at the differences in free field in water with different viscosity in Fig. 20(b). As expected, the frequency response shows a drop at a lower frequency if the viscosity is increased. The same behavior has been observed in air and shown in Fig. 5. Importantly, we underline that in the numerical implementation of the model for the underwater case we cannot calculate the acoustic wavenumber k and the thermal attenuation σ through the approximated expressions in Eqs. (19) and (20), which are valid only for weak viscosity and weak thermal conductivity. Instead, we have to directly solve the fourth degree characteristic equation by numerical methods.

Aliev et al. [30], explained the high underwater efficiency of the carbon nanotubes thermophone through the hydrophobic behavior of the nanotubes. Therefore, we consider here a thin air layer between the thermophone and the water, as seen in Fig. 19. The first result is shown in Fig. 20, where an increase of 55 dB can been observed with respect to the free field response in water. Moreover, a resonance around 15 MHz is also observed and is due to the air gap width between thermophone and water. Now, to better understand the band pass response for mid to low frequency, we can consider Fig. 21, where the response of the system is shown as function of the air gap L_g (three different values of L_g have been adopted). Here, the equation elaborated by Tong et al. [31].

$$p_{\mathrm{rms,NF}} = \left| \frac{1}{\sqrt{2}} \frac{P_{\mathrm{in}}}{2A} (\gamma - 1) \sqrt{\frac{\mathrm{i}\omega}{\alpha_g}} \frac{\kappa_g}{C_{0,g}} \frac{\frac{\mathrm{e}^{k_g L_g}}{\mathrm{e}^{2k_g L_g} - 1} \mathbf{T}\, \mathrm{e}^{\frac{\mathrm{i}\omega}{C_{0,w}}(L_g - x)}}{\beta_s + \kappa_g \sqrt{\frac{\mathrm{i}\omega}{\alpha_g}} + \frac{\mathrm{i}\omega}{2} C_s} \right|, \tag{75}$$

where $\mathbf{T}$ is the transmission coefficient

$$\mathbf{T} = \frac{2\rho_w C_{0,w}}{\rho_g C_{0,g} + \rho_w C_{0,w}}, \tag{76}$$

is also plotted for comparison. This equation was elaborated to describe an encapsulated thermophone with a perfectly rigid backing and with transmission through a window. Then, it has been adapted here to our hydrophobic behavior. Equation (75) assumes that the air gap is large enough so that there is no influence at the air/water interface due to the thermal layer. Fig. 21 shows that, with different gaps, for a high enough frequency the multilayer model agrees with the Tong et al. model. The transition frequency, at which the two models start to concur, is the frequency for which the thermal layer becomes small enough to confine the entire sound generation in the air gap. The slope observed in the high frequency regime is then due to the transmission coefficient between two regions with a high impedance contrast. Below this high frequency regime there is a flat frequency response until a drop for low frequencies. This drop is due to the water on the other side of the thermophone, which acts as an imperfect reflecting substrate. To easily improve the sound generation in a direction, one can use a rigid backing on the other side, which creates a flatter frequency response at low frequencies. The SPL plateau observed for different values of L_g in Fig. 21 is coming from a similar sound generation as the free field plateau response (see Fig. 20). In this case, the air thermal layer oversteps the air-water interface, thus generating a sort of second active layer in the water region. Clearly, this couple of

thermal layers is more efficient than the single thermal layer observed in the case without air gap. Lastly, it is seen that the overall SPL is increased at low frequency for smaller gap size, while diminishing the high frequency response. It means that the increasing of the gap induces a larger SPL in a frequency range which becomes narrower and more shifted towards the low frequencies. This leads us to believe that in order to improve the underwater sound generation we need either to generate the whole sound in the air gap (and so have a large air gap) for low frequencies, or, to have a small air gap so that the thermal layer generates sound also at the air/water interface for higher frequencies. Since the width of the air gap strongly modifies the band pass frequency response of this system, a compromise between frequency range and produced SPL must be accepted, and L_g can be selected depending on the applications of interest. Finally, it has to be kept in mind that a low pass filter response could be achieved for a solid/air/thermophone/air/water design (rigid backing on one hand of the system).

7. Conclusions

In this work the general theory of the thermoacoustic effect has been elaborated for an arbitrary multilayered structure composed of fluid and solid layers. In this system we studied the propagation of the coupled thermal and acoustic waves, by considering the viscous and thermal dissipation. An important point introduced in this approach is that the full thermo-acoustic wave propagation has been considered also in the solid layers, contrarily to classical models where only a form of heat balance is used in the generating thermophone layers or in substrates. Moreover, we provided evidence that the equations for the solid layers and for the fluid layers can be written in the same mathematical form, reducing the complexity of the implemented procedure. The complete system of equations were then solved and rewritten in a matrix form in order to create a flexible and adaptable model allowing for the analysis of different thermophone configurations.

It is important to underline the limitations of our approach. At the interface between the thermophone layer and the adjacent medium we can have an energy loss due to conduction, convection and radiation. These terms are not included in the standard version of our model. However, we can add a term describing the energy loss in the interface conditions. We have described this point in Section 4.1, and more specifically through Eqs. (63) and (64). We remark that this term is represented by an energetic contribution proportional to the local temperature and therefore is well adapted to describe the conduction and convection losses. On the other hand, radiation losses can be considered only with certain approximations since they are typically proportional to the fourth power of the temperature. Another important hypothesis considered in our model is that we work with plane waves in a one-dimensional geometry. This is reasonable only for planar thermophone and for near field conditions. Interestingly enough, the procedure here adopted can be generalized to two-dimensional (cylindrical) and three-dimensional (spherical) geometries. In these cases, the solutions are given by Bessel functions and the results will be discussed in a future work. Concerning the near field assumption, when we need to calculate the acoustic field in an arbitrary position of the space, we can always apply the acoustic diffraction theory based on the near field velocity calculated with our model. This approach has been implemented in Section 5 to draw comparison with experiments.

Three classical thermophone configurations were analyzed and compared with other theoretical models from the literature. In particular, we studied a thermophone in free field, a thermophone deposited on a substrate and a thermophone over a substrate with an air gap in-between. The analysis has displayed good agreement between the presented model and other ones. It has been shown that in order to obtain the highest SPL in air, the thermophone over a substrate with an air gap design should be used. However, due to the size of the thermal length, it is important to leave a large enough air gap between thermophone and substrate to avoid any heat loss, specially at low frequencies.

In order to validate the present approach, we also compared our results with experiments discussed in the recent literature. We compared the theory with the measurements carried out on three different thermophone materials, namely single-layer MWNT sheets, ITO-coated PAN sheets and FDGF sheets. The good agreement showed that the model is able to represent the behavior of systems with values of the heat capacity per unit area varying over several order of magnitude. Moreover, these materials have been used in different configurations, showing the capability of the model to represent the behavior of an arbitrary configuration.

In addition, we also discussed the behavior of two novel thermophone configurations, which can be adopted in air and underwater, respectively. In the first case, we investigated the possibility to create a generation device through two thermophone layers separated by a given air gap. This technique can be profitably used to reduce the density power, thus limiting possible thermophone damages, by increasing at the same time the sound pressure level. In the second case, we discussed the possible underwater use of the thermophone. We analyzed the response of the underwater thermophone in free field and the response of the underwater thermophone with air gaps between generating layer and water. We showed that this last configuration, easily created thank to the hydrophobicity of some nanomaterials, exhibits a very good efficiency and a pass band response which can be controlled by the air gap width.

To conclude, the proposed approach will be useful to explore the thermal behavior and the frequency response of new thermophone configurations, in order to improve the acoustic efficiency and to test the possible exploitation of new materials and/or nanomaterials.

Acknowledgment

This work was supported by the French DGA/MRIS (Direction Générale de l'Armement/Mission pour la Recherche et l'Innovation Scientifique) and is part of a project developed in collaboration with CINTRA, UMI 3288 CNRS/NTU/THALES (Singapore).

References

[1] P. de Lange, On thermophones, Proc. Roy. Soc. Lond. 91 (1915) 239–241.
[2] H.D. Arnold, I. B Crandall, The thermophone as a precision source of sound, Phys. Rev. 10 (1917) 22–38.
[3] E.C. Wente, A condenser transmitter as a uniformly sensitive instrument for the absolute measurement of sound intensity, Phys. Rev. 10 (1917) 39–63.
[4] E.C. Wente, The thermophone, Phys. Rev. 19 (1922) 333–345.
[5] H. Shinoda, T. Nakajima, K. Ueno, N. Koshida, Thermally induced ultrasonic emission from porous silicon, Letters to Nature 400 (1999) 853–855.
[6] A.E. Aliev, N.K. Mayo, R.H. Baughman, D. Avirovik, S. Priya, M.R. Zarnetske, J.B. Blottman, Thermal management of thermoacoustic sound, Nanotechnology 25 (2014) 405704.
[7] A.R. Barnard, T.A. Brungart, T.E. McDevitt, A.E. Aliev, D.M. Jenkins, B.L. Kline, R.H. Baughman, Advancements toward a high-power, carbon nanotube, thin-film loudspeaker, Noise Control Eng. J. 62 (2014) 360–367.
[8] A. Niskanen, J. Hassel, M. Tikander, P. Maijala, L. Gronberg, P. Helisto, Suspended metal wire array as a thermoacoustic sound source, Appl. Phys. Lett. 95 (2009) 163102.
[9] R. Dutta, B. Albee, W.E. Van Der Veer, T. Harville, K.C. Donovan, D. Papamoschou, R.M. Penner, Gold nanowire thermophones, J. Phys. Chem. C 118 (2014) 29101–29107.
[10] H. Tian, D. Xie, Y. Yang, T.L. Ren, Y.X. Lin, Y. Chen, Y.F. Wang, C.J. Zhou, P.G. Peng, L.G. Wang, L.T. Liu, Flexible, ultrathin, and transparent sound-emitting devices using silver nanowires film, Appl. Phys. Lett. 99 (2011) 253507.
[11] H. Tian, T.L. Ren, D. Xie, Y.F. Wang, C.J. Zhou, T.T. Feng, D. Fu, Y. Yang, P.G. Peng, L.G. Wang, L.T. Liu, Graphene-on-paper sound source devices, ACS Nano 5 (2011) 4878–4885.
[12] T.S. Ashton, A.L. Moore, Three-dimensional foam-like hexagonal boron nitride nanomaterials via atmospheric pressure chemical vapor deposition, J. Mater. Sci. 50 (2015) 6220–6226.
[13] M. Loeblein, R.Y. Tay, S.H. Tsang, W.B. Ng, E.H.T. Teo, Configurable three-dimensional boron nitride-carbon architecture and its tunable electronic behavior with stable thermal performances, Small 10 (2014) 2992–2999.
[14] L. Xiao, Z. Chen, C. Feng, L. Liu, Z.Q. Bai, Y. Wang, L. Qian, Y. Zhang, Q. Li, K. Jiang, S. Fan, Flexible, stretchable, transparent carbon nanotube thin film loudspeakers, Nano Lett. 8 (2008) 4539–4545.
[15] M. Daschewski, R. Boehm, J. Prager, M. Kreutzbruck, A. Harrer, Physics of thermo-acoustic sound generation, J. Appl. Phys. 114 (2013) 114903.
[16] M. Daschewski, M. Kreutzbruck, J. Prager, Influence of thermodynamic properties of a thermo-acoustic emitter on the efficiency of thermal airborne ultrasound generation, Ultrasonics 63 (2015) 16–22.
[17] C.S. Kim, S.K. Hong, J.M. Lee, D.S. Kang, B.J. Cho, J.W. Choi, Free-standing graphene thermophone on a polymer-mesh substrate, Small 12 (2016) 185–189.
[18] P. La Torraca, L. Larcher, M. Bobinger, P. Pavan, B. Seeber, P. Lugli, Physical modeling and characterization of thermo-acoustic loudspeakers made of silver nano-wire films, J. Appl. Phys. 121 (2017) 214502.
[19] F.A. McDonald, G.C.J. Wetsel, Generalized theory of the photoacoustic effect, J. Appl. Phys. 49 (2008) 2313.
[20] H. Hu, T. Zhu, J. Xu, Model for thermoacoustic emission from solids, Appl. Phys. Lett. 96 (2010) 214101.
[21] H. Hu, Z. Wang, H. Wu, Y. Wang, Analysis of spherical thermo-acoustic radiation in gas, AIP Adv. 2 (2012) 032106.
[22] H. Hu, D. Wang, Z. Wang, Solution for acoustic field of thermo-acoustic emission from arbitrary source, AIP Adv. 4 (2014) 107114.
[23] Y. Yin, H. Hu, Analysis of cylindrical thermo-acoustic radiation in gas, AIP Conference Proceedings 1829 (2017) 020033.
[24] H. Hu, Y. Wang, Z. Wang, Wideband flat frequency response of thermo-acoustic emission, J. Phys. D Appl. Phys. 45 (2012) 345401.
[25] C.W. Lim, L.H. Tong, Y.C. Li, Theory of suspended carbon nanotube thin film as a thermal-acoustic source, J. Sound Vib. 332 (2013) 5451–5461.
[26] L.H. Tong, C.W. Lim, S.K. Lai, Y.C. Li, Gap separation effect on thermoacoustic wave generation by heated suspended CNT nano-thinfilm, Appl. Therm. Eng. 86 (2015) 135–142.
[27] Y.S. Liu, L.H. Tong, S.K. Lai, Thermo-acoustics generated by periodically heated thin line array, J. Sound Vib. 427 (2018) 28–40.
[28] V. Vesterinen, A.O. Niskanen, J. Hassel, P. Helisto, Fundamental efficiency of nanothermophones: modeling and experiments, Nano Lett. 10 (2010) 5020–5024.
[29] J.J. Brown, N.C. Moore, O.D. Supekar, J.C. Gertsch, V.M. Bright, Ultrathin thermoacoustic nanobridge loudspeakers from ALD on polyimide, Nanotechnology 27 (2016) 475504.
[30] A.E. Aliev, M.D. Lima, S. Fang, R.H. Baughman, Underwater sound generation using carbon nanotube projectors, Nano Lett. 10 (2010) 2374–2380.
[31] L.H. Tong, C.W. Lim, Y.C. Li, Gas-filled encapsulated thermal-acoustic transducer, J. Vib. Acoust. 135 (2013) 051033.
[32] A.E. Aliev, Y.N. Gartstein, R.H. Baughman, Increasing the efficiency of thermoacoustic carbon nanotube sound projectors, Nanotechnology 24 (2013) 235501.
[33] L. Xiao, P. Liu, L. Liu, Q. Li, Z. Feng, S. Fan, K. Jiang, High frequency response of carbon nanotube thin film speaker in gases, J. Appl. Phys. 110 (2011) 084311.
[34] A.E. Aliev, N.K. Mayo, R.H. Baughman, Y.N. Gartstein, R.H. Baughman, D. Codoluto, R. Ovalle-Robles, K. Inoue, S.A. Romanov, A.G. Nasibulin, P. Kumar, S. Priya, J.B. Blottman, Thermoacoustic sound projector: exceeding the fundamental efficiency of carbon nanotubes, Nanotechnology 29 (2018) 325704.
[35] L.D. Landau, E.M. Lifschitz, third ed., Fluid Mechanics, Course of Theoretical Physics, vol. 6, Butterworths Heinemann, Oxford, 1986.
[36] L.D. Landau, E.M. Lifschitz, third ed., Theory of Elasticity, Course of Theoretical Physics, vol. 7, Butterworths Heinemann, Oxford, 1986.
[37] F. Pavanello, F. Manca, P.L. Palla, S. Giordano, Generalized interface models for transport phenomena: unusual scale effects in composite nanomaterials, J. Appl. Phys. 112 (2012) 084306.
[38] F. Pavanello, S. Giordano, How imperfect interfaces affect the nonlinear transport properties in composite nanomaterials, J. Appl. Phys. 113 (2013) 154310.
[39] P. La Torraca, M. Bobinger, M. Servadio, P. Pavan, M. Becherer, P. Lugli, L. Larcher, On the frequency response of nanostructured thermoacoustic loudspeakers, Nanomaterials 8 (2018) 833.
[40] Ali E. Aliev, Nathanael K. Mayo, Monica Jung de Andrade, Raquel O. Robles, Shaoli Fang, Ray H. Baughman, Mei Zhang, Yongsheng chen, Jae Ah Lee, Seon Jeong Kim, Alternative nanostructures for thermophones, ACS Nano 9 (2015) 4743–4756.
[41] Wenwen Fei, Jianxin Zhou, Wanlin Guo, Low-voltage driven graphene foam thermoacoustic speaker, Small 11 (2015) 2252–2256.